# Chapter 3

Electronic Structures and Energetics of Tetraamido Macrocyclic Ligated Iron Complexes

3.1 Introduction

Non-heme mononuclear and dinuclear complexes are involved in many catalytic reactions such as C-H activation, oxygen transfer, alcohol oxidation, deformylation reactions.[1-7] C-H bond activation in hydrocarbons is highly inert and biomimetic species can provide a direct way to introduce functional groups, cost-effectively, and has high industrial applications.[8-10] C-H bond activation is inspired by models of Cyt P450 and Rieske dioxygenase, and these hydroxylate unactivated C-H bonds with higher selectivity at fast rates.[11-12] Selective functionalization of C-H bond in organic compounds is a "grand challenge" in catalysis science.[13-18] To carry out selective C-H bond activation, many heme,[19-21] and non-heme[22-29] iron-containing complexes have been used with dioxygen as an oxidant. Dioxygen (O_2) is an ideal oxidant due to several reasons as it is abundant in nature, a renewable chemical oxidant, water as a byproduct, non-toxic at most of the conditions, and its reduction potential are more than sufficient to carry many chemical transformations.[30-35] Non-heme complexes with tetradentate N-atom donor ligand having *cis* labile sites (FeN_4) show great promise for selective C-H bond activation.[36-39] As iron is ubiquitous, has low toxicity and can exist in multiple redox states make its chemistry interseting and acts as a key intermediate in many biotransformation reactions, occurring via C-H, O-H activation, including biological O_2 activation, etc.[40-45]

Tetraamido macrocyclic ligand (TAML) activator is widely used in chemical and biological agents such as petroleum refining, water treatment, textiles, cleaning, etc.[46] TAML activators have about 10000 turnovers per hour in many applications.[47] The TAML coordinated metal species being environment friendly have been tested.[48] To investigate the catalytic properties, many experimental and theoretical studies such as Mossbauer, EPR, density functional theory (DFT), transient and steady-state kinetics have been used.[39,49-50] Last two decades,

tetradentate TAML ligated iron species becomes a popular oxidant to achieve an effective small biomimetic molecule of oxidizing enzymes for green oxidation chemistry.[30,51] It has biological elements like C, H, N, O, and Fe, and is devoid of toxic functionalities.[52] There are several Fe-TAML complexes such as mononuclear iron oxo/peroxo/superoxo/hydroperoxo as well as oxygen bridged dinuclear species that are observed in previous literature.[50,53-56] Some of the species are also well characterized by X-rays and spectroscopic parameters.[49,50,57] These species are also important intermediates generated during various metal-mediated catalytic transformation reactions such as alkane hydroxylation, olefin epoxidation, and sulfoxidation[58-74] occurring via C-H bond activation. These reactions are also important in synthetic pharmaceutical[75] and biological processes such as medicine, photosystem-II, naphthalene dioxygenase, etc.[76-77]
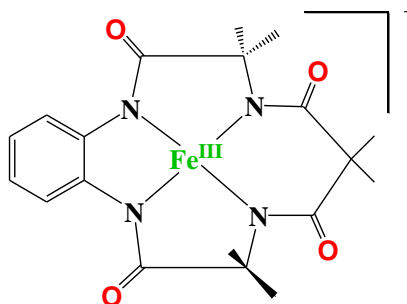
Scheme 3.1. A schematic diagram of tetraamido macrocyclic ligand coordinated iron $[Fe^{III}(TAML)]^-$ species.[39,50]

The growing interest in TAML ligated iron species motivated us to explore structures and spin-state energetics of mononuclear oxo/peroxo/superoxo/hydroperoxo and oxygen bridged dinuclear species as a possible oxidant in many catalytic transformation reactions. Here, we would like to underpin and compare electronic structures, bonding, magnetic interactions, and spin-state energetic aspects of $Fe(III/IV/V)-O/O_2$ and $Fe(IV)-\mu-O_1/O_2-Fe(IV)$-species. By a study of structures and bonding of the species, we also like to comment on their reactivity.

3.2 Computational Details

All calculations are carried out by using Gaussian09 programs.[78] In earlier work, DFT calculations have performed on iron species employing B3LYP, B3LYP-D2, wB97XD, B97D, M06-2X, OLYP, TPPSh, and MP2 methods.[71,73] Among the tested functional, B3LYP incorporating dispersion correction (B3LYP-D2 functional) was found to be superior in predicting the correct spin ground state of iron species.[71,73] So here, we have restricted geometry optimizations using only B3LYP-D2 functional.[79] The LACVP basis set comprising the LanL2DZ-Los Alamos effective core potential for the iron[80-82] and a 6-31G[83] basis set for the other atoms (C, H, N, and O) have been employed for geometry optimization. To identify the geometry is located at the lowest point on the potential energy surface is made by frequency calculations which are performed on optimized geometry and confirmed by the absence of imaginary frequencies, free energy corrections are also found by frequency calculation. Single point energy calculations are made by using a TZVP[76,84-85] basis set on all-atoms of the optimized geometries. For computing the solvation energies using acetonitrile as a solvent, PCM solvation model is used. The quoted DFT energies are B3LYP-D2 solvation including free-energy corrections with TZVP basis set at the temperature of 298.15 K. From the optimized geometries, structural parameters, vibrational wavenumbers, and other molecular properties like HOMO-LUMO and NBO are analyzed. The vibrational energy distribution analysis (VEDA) program is used to calculate the partial energy distribution (PED),[86] by using PED fundamental vibrational modes are characterized. Theoretical and valuable information about intra and intermolecular charge transfer (ICT), conjugation and hyperconjugation of the molecular system[87-88] are provided by natural bonding orbital (NBO) analysis. Using the Mulliken population analysis (MPA) method with B3LYP-D2 functional charges on the atoms of complexes are calculated. In the Gaussian09 fragment approach available which is employed to aid smooth convergence. In the diiron species, the magnetic

exchange between both the iron centers is calculated by employing the following spin Hamiltonian,

$$\hat{H} = -J\,S_1.S_2$$

Where J is the magnetic exchange coupling constant, the positive J value shows the ferromagnetic coupling while negative J values show the antiferromagnetic coupling. Noodleman's broken symmetry is used to compute the magnetic exchange coupling (J) constant.[89-90] Common notation of $^{mult}A_{spin\ state}$ is used throughout where the mult, A, and spin state denote the total multiplicity, the species, and the possible spin states respectively.

3.3 Results and Discussion

Here, we will thoroughly discuss electronic structures, bonding nature and spin state energetics of biomimetic $[Fe^{III}(TAML)]^-$ (species I) and its possible mononuclear derivatives end on $[(TAML)Fe^{IV}-\eta^1-O_2]^{\bullet-}$ (species II), side on $[(TAML)Fe^{IV}-(\eta^2-O_2)]^{2-}$ (species IIIa), $[(TAML)Fe^{III}-(\eta^2-O_2)]^{3-}$ (species IIIb), $[(TAML)Fe^{IV}-OOH]^-$ (species IV), $[(TAML)Fe^{IV}-O]^{2-}$ species (V), $[(TAML)Fe^{V}-O]^-$ species (VI), and dinuclear derivaties $[(TAML)Fe^{IV}-\mu O-(TAML)Fe^{IV}]^{2-}$ (species VII) and $[(TAML)Fe^{IV}-\mu O_2-Fe^{IV}(TAML)]^{2-}$ (species VIII) followed by comparative study.

3.3.1 Electronic structure and energetics of $[Fe^{III}(TAML)]^-$ (species I)

It is a tetraamido macrocyclic species containing iron ions, is a very efficient and selective catalyst.[22-29] In species I, iron is surrounded by four deprotonated N-amido ligands and is almost square planar species.[39] This is well characterized by X-ray, UV-vis, EPR, and EXAFS.[39] We have optimized species I on the surfaces of S=5/2 (sextet; $^6I_{hs}$) and S=3/2

(quartet; $^4I_{is}$), and our DFT calculations reveal that the quartet state is computed to be the ground state, and the sextet state lies at 89.0 kJ/mol higher in energy (see Figure 3.1).
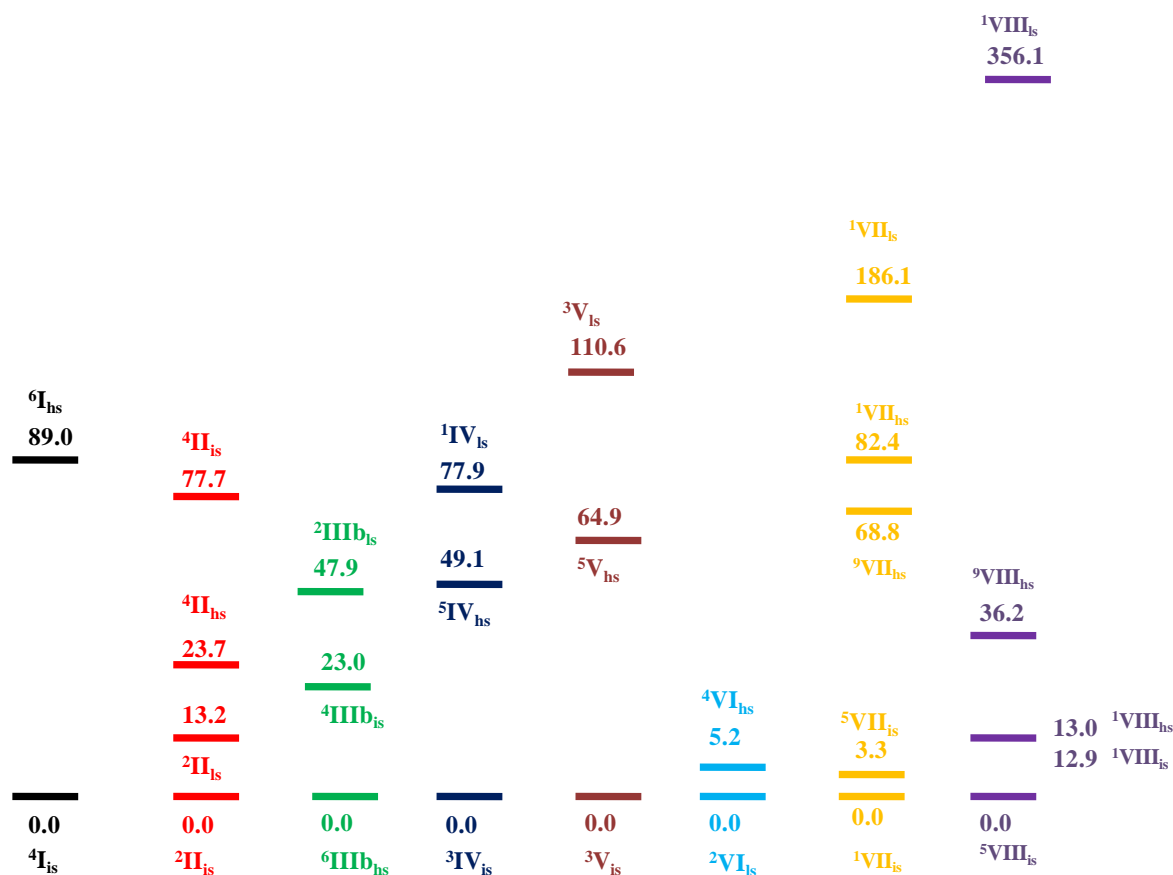

Figure 3.1. B3LYP-D2 computed relative energies (in kJ/mol) of species I-VIII.

This ground state is also supported by the experimental report.[39] The computed Fe-N$_{avg}$ bond length of the ground state is found to be 1.865 Å and this is in good agreement with the X-ray structure (see Table 3.1).[39] A spin density of $\rho = 2.663$ is located at the iron center (see Table 3.2). The optimized structure of ground state and the corresponding spin density plot is shown in Figure 3.2(a,b). The electronic configuration at the metal center is found to be $(d_{yz})^2$, $(d_{xz})^1$, $(d_{z^2})^1$, $(d_{xy,})^1$ and $(d_{x^2-y^2})^0$ (see Figure 3.3).

Table 3.1. B3LYP-D2 computed selective structural parameters of species I-VIII.

	Bond length (Å)									Bond angle (°)				
Spin States	Fe-N$_1$	Fe-N$_2$	Fe-N$_3$	Fe-N$_4$	Fe1-N$_{av}$	Fe1-N$_{av}$	Fe-O1	Fe-O2	O1-O2	N$_1$-Fe-N$_3$	N$_4$-Fe-N$_1$	Fe-O1-O2	Fe$_2$-O$_2$-O$_1$	Fe1-O1-Fe2
^{6}I$_{hs}$	1.984	1.983	1.924	1.924	1.953	-	-	-	-	159.7	159.7	-	-	-
^{4}I$_{is}$	1.864	1.864	1.867	1.867	1.865	-	-	-	-	171.9	171.9	-	-	-
Exp.[39]	1.881	1.876	1.892	1.889	1.884									
^{4}II$_{hs}$	1.876	1.876	1.881	1.881	1.878	-	2.121	-	1.321	162.1	162.1	117.3	-	-
^{4}II$_{is}$	1.873	1.873	1.872	1.871	1.872	-	2.001	-	1.325	160.9	160.9	119.1	-	-
^{2}II$_{is}$	1.877	1.877	1.877	1.877	1.877	-	2.173	-	1.296	162.7	162.7	118.5	-	-
^{2}II$_{ls}$	1.877	1.877	1.883	1.882	1.879	-	1.963	-	1.321	160.2	160.2	121.7	-	-
^{6}III$_{hs}$	2.127	2.058	2.093	2.096	2.093	-	1.994	2.009	1.537	128.8	133.5	-	-	-
^{4}III$_{is}$	2.176	2.119	1.990	2.053	2.084	-	1.953	1.973	1.508	127.1	132.9	-	-	-
^{2}III$_{ls}$	1.980	1.978	1.988	1.985	1.983	-	1.954	1.952	1.516	129.2	150.8	-	-	-
Exp.[56]							1.927							
^{5}IV$_{hs}$	1.887	1.915	1.906	1.883	1.898	-	2.028	-	1.482	159.4	158.1	113.9	-	-
^{3}IV$_{is}$	1.881	1.875	1.884	1.889	1.882	-	1.889	-	1.486	156.4	155.3	112.5	-	-
^{1}IV$_{ls}$	1.876	1.893	1.866	1.878	1.878	-	1.756	-	1.522	154.0	156.5	115.1	-	-
^{5}V$_{hs}$	1.953	1.986	1.981	2.066	1.996	-	1.680	-	-	148.3	134.8	-	-	-
^{3}V$_{is}$	1.912	1.912	1.911	1.911	1.911	-	1.653	-	-	152.9	152.9	-	-	-
^{1}V$_{ls}$	1.943	1.874	1.944	1.866	1.906	-	1.657	-	-	159.3	144.5			
Exp.[29]					1.86		1.64							
^{4}VI$_{hs}$	1.914	1.914	1.878	1.878	1.896	-	1.664	-	-	155.7	155.8	-	-	-
^{2}VI$_{hs}$	1.898	1.898	1.887	1.886	1.892	-	1.630	-	-	152.2	152.1	-	-	-

Exp.[50]					1.87		1.59							
[9]VII$_{hs}$	-	-	-	-	1.917	1.917	1.860	1.860	-	-	-	-	-	169.8
[I]VII$_{hs}$	-	-	-	-	1.913	1.895	1.834	1.711	-	-	-	-	-	160.5
[5]VII$_{is}$	-	-	-	-	1.904	1.903	1.800	1.801	-	-	-	-	-	167.6
[1]VII$_{is}$	-	-	-	-	1.913	1.895	1.835	1.711	-	-	-	-	-	160.5
[1]VII$_{ls}$	-	-	-	-	1.891	1.885	1.704	1.744	-	-	-	-	-	149.4
Exp.[55]					1.89		1.74							
[9]VIII$_{hs}$	-	-	-	-	1.882	1.886	2.261	2.256	1.330	-	-	118.3	118.1	
[I]VIII$_{hs}$	-	-	-	-	1.890	1.884	2.115	2.078	1.370	-	-	113.1	112.7	
[5]VIII$_{is}$	-	-	-	-	1.882	1.883	2.124	2.127	1.334	-	-	116.4	116.3	
[1]VIII$_{is}$	-	-	-	-	1.891	1.884	2.078	2.115	1.370	-	-	113.1	112.7	
[1]VIII$_{ls}$	-	-	-	-	1.879	1.878	1.756	1.759	1.472	-	-	113.9	115.1	

Table 3.2. B3LYP-D2 computed spin density values of the species I-VIII.

Spin states	Fe1	Fe2	O`1	O2
$^6\mathrm{I_{hs}}$	3.914	-	-	-
$^4\mathrm{I_{is}}$	2.663	-	-	-
$^2\mathrm{I_{ls}}$	1.187	-	-	-
$^4\mathrm{II_{is}}$	0.984	-	0.548	0.771
$^2\mathrm{II_{is}}$	2.586	-	-0.703	-0.881
$^2\mathrm{II_{ls}}$	-1.029	-	0.591	0.771
$^6\mathrm{IIIb_{hs}}$	3.887	-	0.315	0.338
$^4\mathrm{IIIb_{is}}$	3.018	-	-0.443	-0.327
$^2\mathrm{IIIb_{ls}}$	1.089	-	-0.060	-0.057
$^5\mathrm{IV_{hs}}$	2.591		0.446	0.101
$^3\mathrm{IV_{is}}$	2.109		-0.104	-0.026
$^1\mathrm{IV_{ls}}$	0		0	0
$^5\mathrm{V_{hs}}$	3.087	-	0.576	-
$^3\mathrm{V_{is}}$	1.347	-	0.584	-
$^1\mathrm{V_{ls}}$	0	-	0	-
$^4\mathrm{VI_{hs}}$	1.279	-	0.757	-
$^2\mathrm{VI_{ls}}$	1.061	-	0.585	-
$^9\mathrm{VII_{hs}}$	3.208	3.208	0.876	-
$^1\mathrm{VII_{hs}}$	1.524	-2.351	0.125	-
$^5\mathrm{VII_{is}}$	2.207	2.202	0.261	-
$^1\mathrm{VII_{is}}$	2.351	-1.524	-0.125	-
$^1\mathrm{VII_{ls}}$	0	0	0	-
$^9\mathrm{VIII_{hs}}$	2.662	2.663	0.739	0.738
$^1\mathrm{VIII_{hs}}$	2.512	-2.639	0.498	0.427
$^5\mathrm{VIII_{is}}$	2.593	2.593	-0.584	-0.583
$^1\mathrm{VIII_{is}}$	2.639	-2.511	-0.498	-0.426
$^1\mathrm{VIII_{ls}}$	0	0	0	0

The HOMO-LUMO gap of the ground state is found to be 4.446 eV (see Figure 3.2c). By reaction of $[\mathrm{Fe^{III}(TAML)}]^-$ species with dioxygen can form mononuclear end-on $\{[(\mathrm{TAML})\mathrm{Fe^{IV}}\text{-}\eta^{\,1}\text{-}\mathrm{O_2}]^{\bullet-}\}$/side-on species $\{[(\mathrm{TAML})\mathrm{Fe^{III/IV}}\text{-}\eta^{\,2}\text{-}\mathrm{O_2}]^{3/2-}\}$ or dinuclear μ-oxo$\{[(\mathrm{TAMLFe^{IV}})_2(\mu\text{-oxo})]^{2-}\}$/peroxo $\{[(\mathrm{TAMLFe^{IV}})_2(\mathrm{peroxo(O_2)})]^{2-}\}$bridged species which can also consequently form iron(IV/V)-oxo species.[55] After reactions of species I with

dioxygen, the iron metal center is no longer in the plane but it gets out of the plane due to repulsion between charges of the coordinated nitrogen atoms and the axial ligands, that forces the iron atom out of the plane. The distance of the shift of iron metal out of the plane depends upon the elastic force that drives the iron metal back into the plane is balanced.[39]
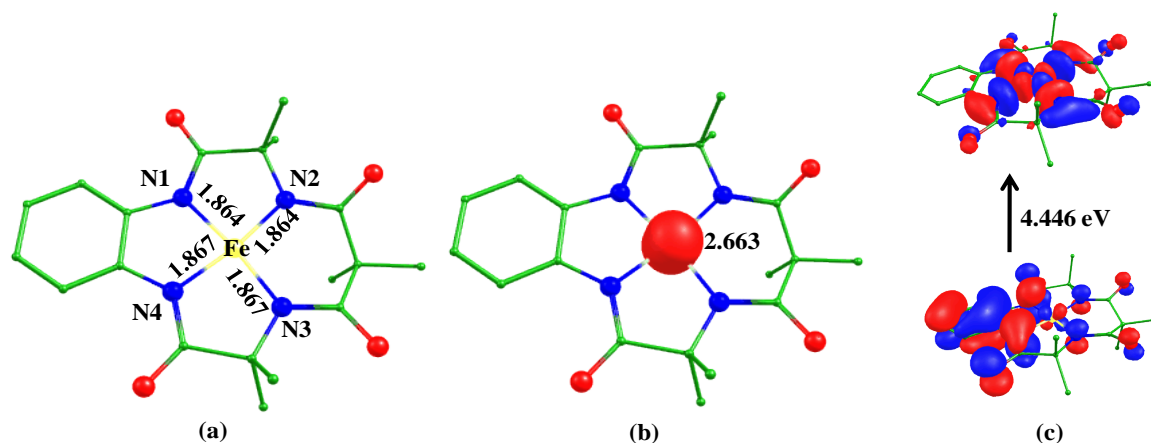

(a) (b) (c)

Figure 3.2. Computed Eigen-value plot incorporating energies computed for *d*-based orbitals for alpha and beta spin corresponding to the ground state ($^4I_{is}$) (energies are given in eV).
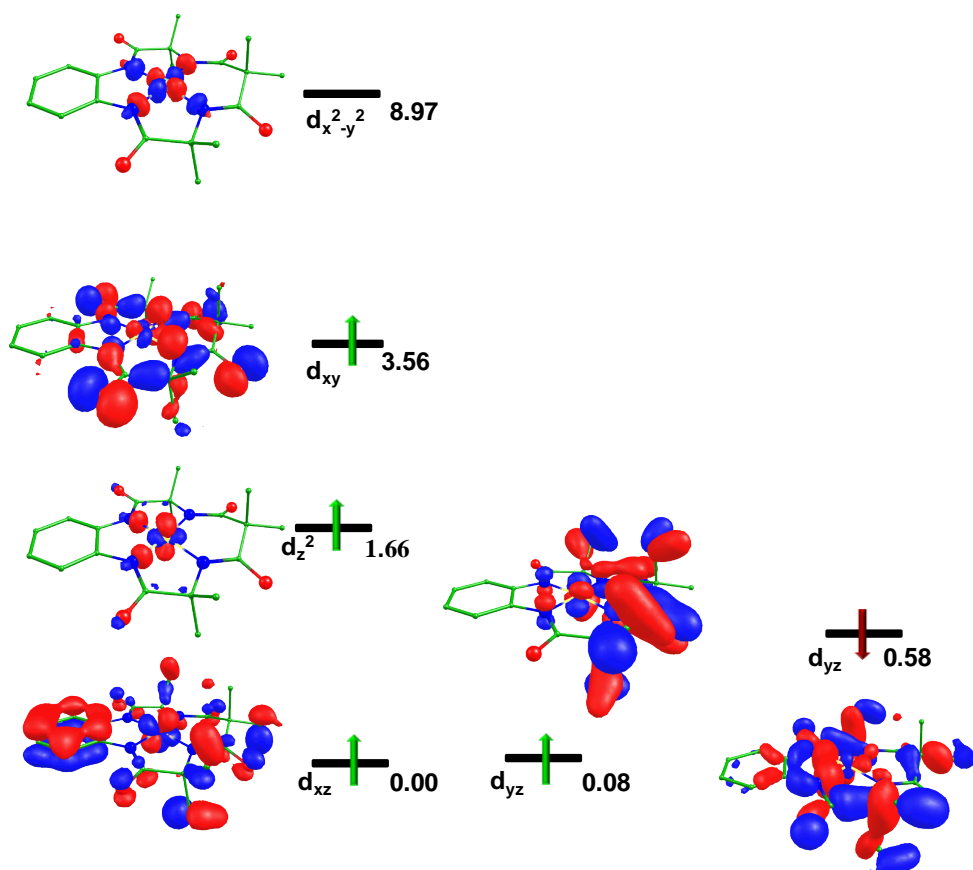
Figure 3.3. B3LYP-D2 a) optimized structure of $^4I_{is}$ (bond length in Å), b) its spin density plot, and c) HOMO-LUMO frontier molecular orbitals of $^4I_{is.}$

3.3.2 Electronic structure and energetics of end-on $[(TAML)Fe^{IV}\text{-}\eta^1\text{-}O_2]^{\bullet-}$ (species II)

When the binding mode of oxygen is η^1 can generate end on iron-superoxo species.[91-92] Five spin interactions can be possible due to the presence of four unpaired electrons at the iron center and one unpaired electron at distal oxygen. We have optimized all spin states of this species except $^6II_{hs}$ (due to the spin convergence issue). The antiferromagnetically coupled intermediate spin state ($^2II_{is}$) is found to be the ground state with the $^4II_{hs}$, $^4II_{is}$, and $^2II_{is}$ lie at 23.8, 77.7, and 13.2 kJ/mol, respectively (see Table 3.3), and the ground state is also inconsistent with similar species in the previous report.[56] The optimized structure and spin density plot of the ground state are shown in Figure 3.4. The average Fe-N_{avg} bond of species II is larger than species I by 0.013 Å.

Table 3.3. Possible electronic configuration for superoxo species II.

	Electronic configuration		
Spin state	**Fe(IV)**	**$O_2^{\bullet-}$**	**Relative energy(kJ/mol)**
$^6II_{hs}$	$\pi^*_{xz}{}^{\uparrow}\ \pi^*_{yz}{}^{\uparrow}\ \delta_{xy}{}^{\uparrow}\ \sigma^*_{z}{}^{\uparrow 2}\ \delta_{x}{}^2{}_{-y}{}^2$	$\Phi^{\uparrow}$	-
$^4II_{hs}$	$\pi^*_{xz}{}^{\uparrow}\ \pi^*_{yz}{}^{\uparrow}\ \delta_{xy}{}^{\uparrow}\ \sigma^*_{z}{}^{\uparrow 2}\ \delta_{x}{}^2{}_{-y}{}^2$	$\Phi^{\downarrow}$	23.7
$^4II_{is}$	$\pi^*_{xz}{}^{\uparrow\downarrow}\ \pi^*_{yz}{}^{\uparrow}\ \delta_{xy}{}^{\uparrow}\ \sigma^*_{z}{}^2\ \delta_{x}{}^2{}_{-y}{}^2$	$\Phi^{\uparrow}$	77.7
$^2II_{is}$	$\pi^*_{xz}{}^{\uparrow\downarrow}\ \pi^*_{yz}{}^{\uparrow}\ \delta_{xy}{}^{\uparrow}\ \sigma^*_{z}{}^2\ \delta_{x}{}^2{}_{-y}{}^2$	$\Phi^{\downarrow}$	0
$^2II_{ls}$	$\pi^*_{xz}{}^{\uparrow\downarrow}\ \pi^*_{yz}{}^{\uparrow\downarrow}\ \delta_{xy}\ \sigma^*_{z}{}^2\ \delta_{x}{}^2{}_{-y}{}^2$	$\Phi^{\uparrow}$	13.2

The Fe-O1 and O1-O2 bond lengths are computed to be 2.173 Å and 1.296 Å. The O1-O2 bond length is in agreement with the other metal-superoxo species that are ca. 1-2-1.3 Å.[92-97]

The stretching frequencies of the Fe-O and O-O bonds are computed to be $\nu 314$ cm^{-1} and $\nu 1200$ cm^{-1} that are also agreed with calculated stretching frequency with other superoxide species.[92-96] The iron center of this species is found to be shifted by 0.08 Å (see Table 3.4) above the plane along with the axial bond concerning species I and this is due to repulsion between charges of equatorial ligated nitrogen atoms and axial superoxo ligands, that forces the iron metal out of the plane, and suggested species II is relatively less planar.
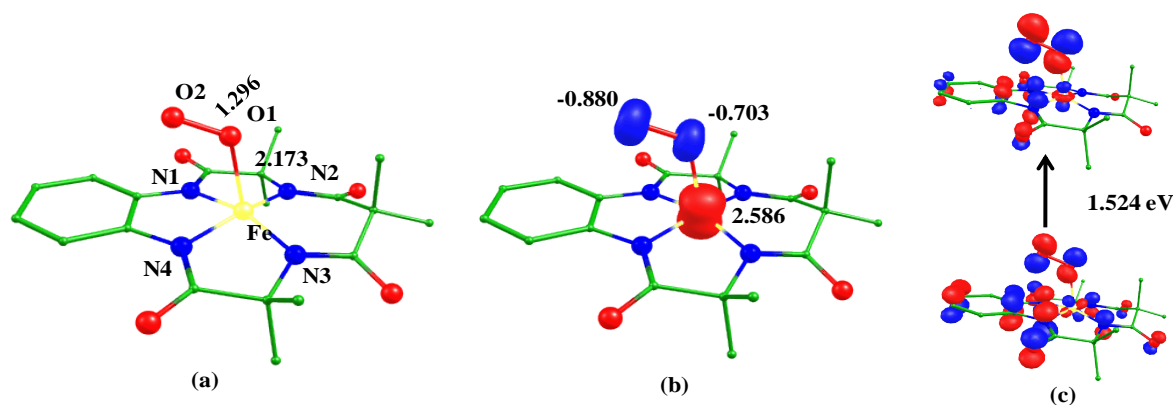
Figure 3.4. B3LYP-D2 a) optimized structure (bond length in Å) of $^2\text{II}_{\text{is}}$, b) its spin density plot and c) The HOMO-LUMO frontier molecular orbitals of $^2\text{II}_{\text{is}}$.

Table 3.4. B3LYP-D2 computed displacement in Z-axis species II-VIII.

Species	Displacement in Z-axis (Å)
$^2\text{II}_{\text{is}}$	0.08
$^6\text{IIIb}_{\text{hs}}$	0.72
$^3\text{IV}_{\text{is}}$	0.19
$^3\text{V}_{\text{is}}$	0.35
$^2\text{VI}_{\text{ls}}$	0.40
$^1\text{VII}_{\text{is}}$	-0.41, 0.42
$^5\text{VIII}_{\text{is}}$	0.04, -0.07

The HOMO-LUMO gap of species II is found to be 1.524 eV (see Figure 3.4c) and the gap is smaller than the species I. The eigenvalue plot of the ground state is shown in Figure 3.5, and

the electronic configuration at the metal center is found to be $(d_{xz})^2$, $(d_{yz})^1$, $(d_{xy,})^1$, $(d_{z^2})^0$ and $(d_{x^2-y^2})^0$. The spin density values at iron and distal oxygen centers are computed to be 2.586 and -0.881 suggest the presence of antiferromagnetic coupling between them and a significant spin density at distal oxygen can activate C-H and O-H bond.[56,61,97]
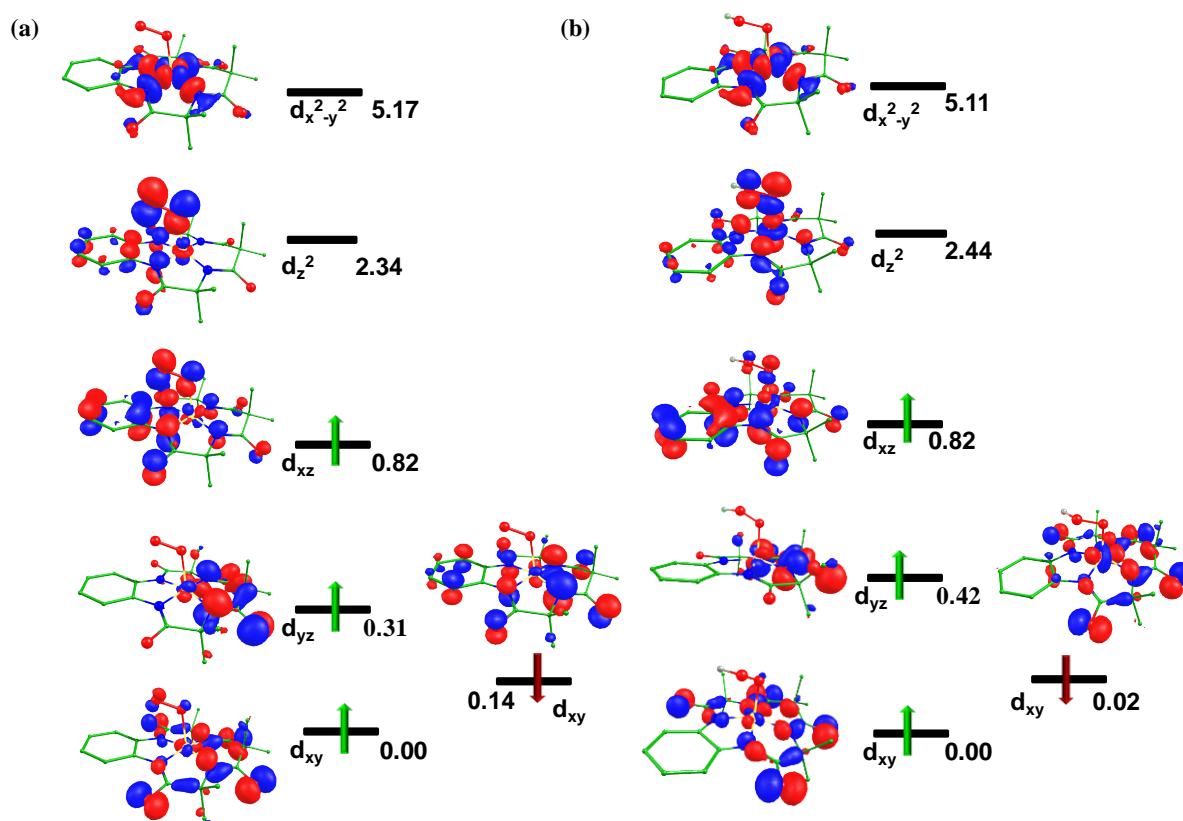

Figure 3.5. Computed eigenvalue plot incorporating energies computed for *d*-based orbitals for alpha and beta spin corresponding to the ground state a) (^{2}II$_{is}$) b) (^{3}IV$_{is}$) (energies are given in eV).

3.3.3 Electronic structure and energetics of side-on [(TAML)Fe^{IV}-(η^2-O$_2$)]$^{2-}$ (species IIIa) and [(TAML)Fe^{III}-(η^2-O$_2$)]$^{3-}$ (species IIIb)

When the binding mode of oxygen is η^2, the side-on species can be formed.[96-97] Similar to species II, we have tried to optimize all three possible spin surfaces (such as ^{5}IIIa$_{hs}$, ^{3}IIIa$_{is}$, and ^{1}IIIa$_{ls}$) of species III but here we have got optimization only at one spin state i.e. the low

spin surface (^{1}IIIa$_{ls}$), and other spin surfaces have found bond cleavage between iron and oxygen atoms. The optimized structure for the low spin is shown in Figure 3.6a, and spin density on the iron center is found to be zero as (S=0). The Fe-N$_{avg}$ bond elongates to 1.904 Å and this is lower than species IIIb and higher than species II (see Table 1). The computed Fe-O1, Fe-O2, and O1-O2 bond lengths are found to be 1.908 Å, 1.906 Å, and 1.478 Å, these are also found to be similar to Mn(III)-peroxo species.[6] The computed stretching frequency of the O1-O2 bond is found to be v945 cm^{-1}, and bond length of the O1-O2 also decreases which shows that O-O bond strength increases with the increase of the oxidation state.[7]

(a)

(b)

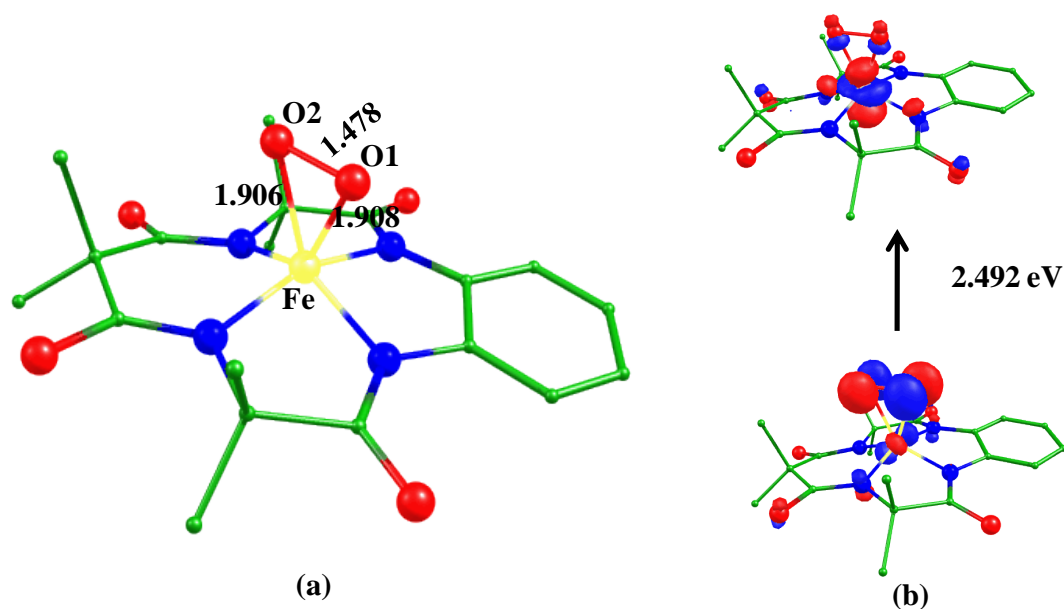**Figure 3.6.** B3LYP-D2 (a) optimized structure (bond length in Å) and (b HOMO-LUMO frontier molecular orbitals) of the low spin state of side-on [(TAML)Fe^{IV}-(η ^{2}-O$_2$)]$^{2-}$ (species IIIa).

The HOMO-LUMO gap is found to be 2.492 eV (see Figure 3.6b). The eigenvalue plot is shown in Figure 3.7, and the electronic configuration of the iron is found to be $(d_{xy})^2$, $(d_{yz})^2$, $(d_{z^2})^0$, $(d_{xz})^0$, and $(d_{x^2-y^2})^0$. This species can also involve in catalytic reactions. So, here we have also taken side-on species with oxidation state +3 at the iron center and attempted to optimize all three possible spin states (^{6}IIIb$_{hs}$, ^{4}IIIb$_{is}$, and ^{2}IIIb$_{ls}$) for the species IIIb. Our DFT

calculations predicted that the sextet spin state (^{6}IIIb$_{hs}$) is found to be the ground state with ^{4}IIIb$_{is}$ and ^{2}IIIb$_{ls}$ lie at 23.0 and 47.9 kJ/mol, respectively.
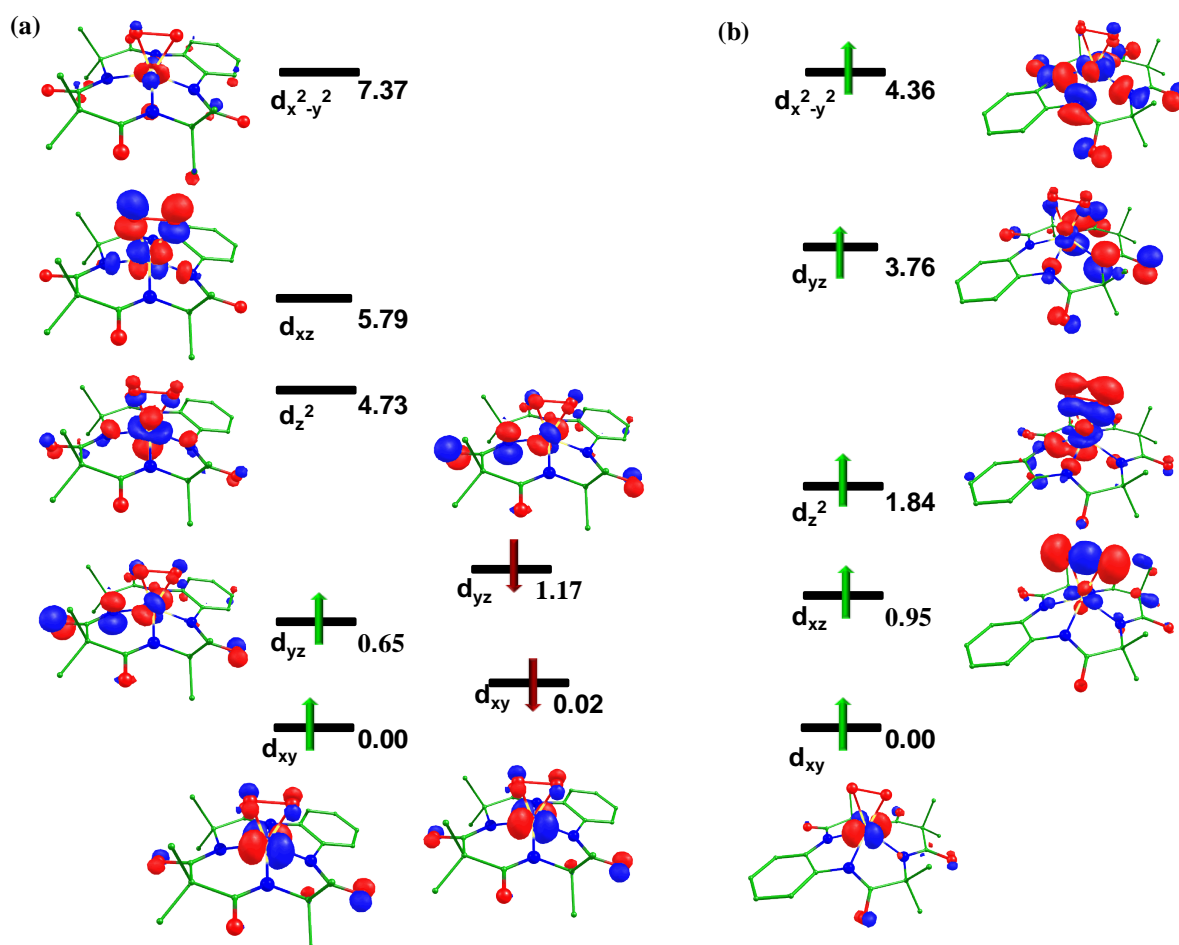

Figure 3.7. Computed Eigenvalue plot incorporating energies computed for *d*-based orbitals for alpha and beta spin corresponding to the a) (^{1}III$_{ls}$a) (energies are given in eV); b) ground state (^{6}IIIb$_{hs}$) (energies are given in eV).

The optimized structure and spin density plot of the ground state is shown in Figure 3.8a,b. The Fe-N$_{avg}$ bond is computed to be 2.093 Å and this is higher than the species II. The computed Fe-O1 and Fe-O2 bond lengths are 2.009 Å and 1.994 Å which are also observed in similar architecture.[98] Computed parameters suggest that the oxygen binds with iron symmetrically. The iron oxygen bond length is found to be smaller while the O1-O2 bond length is slightly higher than the end-on species II and these are also confirmed by the

computed stretching frequency of Fe-O ($v448$ cm^{-1}) and O-O ($v821$ cm^{-1}) bond.[95] The computed bond angle of O1-Fe-O2 is found to be 45.1° indicates the pseudo square pyramidal geometry of species IIIb. The shift in the position of the iron atom is computed to be 0.72 Å (see Table 3.4).
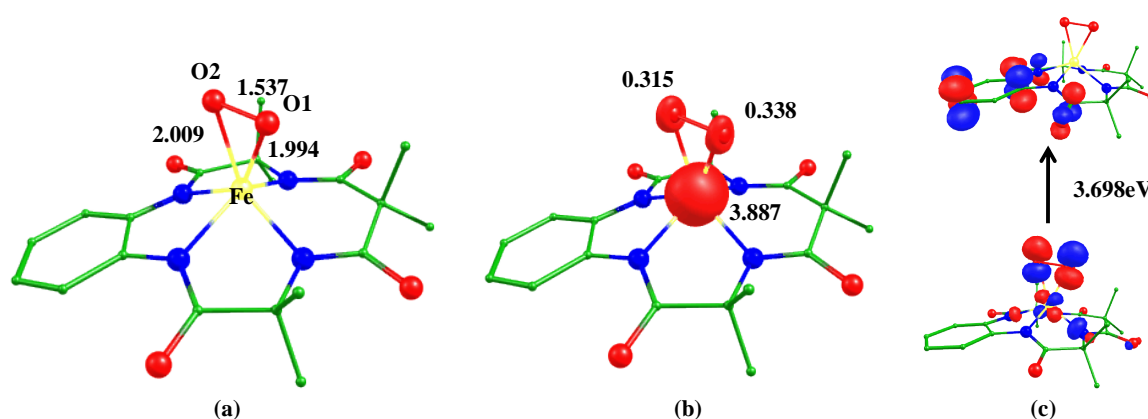

Figure 3.8. B3LYP-D2 a) optimized structure (bond length in Å), b) spin density plot of ^{6}IIIb$_{hs}$ and c) The HOMO-LUMO frontier molecular orbitals of ^{6}IIIb$_{hs}$.

The spin density value of 3.887 is located at the iron center and both the oxygen atoms occupied similar spin density that indicates symmetrical binding mode (see Figure 3.8b). The eigenvalue plot of the ground state is shown in Figure 3.7b. The electronic configuration on Fe metal is found to be $(d_{xy})^1$, $(d_{xz})^1$, $(d_{yz})^1$, $(d_{z^2})^1$, and $(d_{x^2-y^2})^1$. The HOMO-LUMO gap of species IIIb is calculated to be 3.698 eV (see Figure 3.8c), and this is greater than species II may indicate the possibility of lesser electron transfer compared to species II. The significant spin densities at both the oxygen atoms indicates that they can participate in catalytic reactions.[61-64] The NBO plots of the ground state show that orbital contributions between both the oxygen atoms and iron center are involved in making σ-bond confirmed the presence of σ-bond between both the oxygen atoms and iron center (see Figure 3.9).
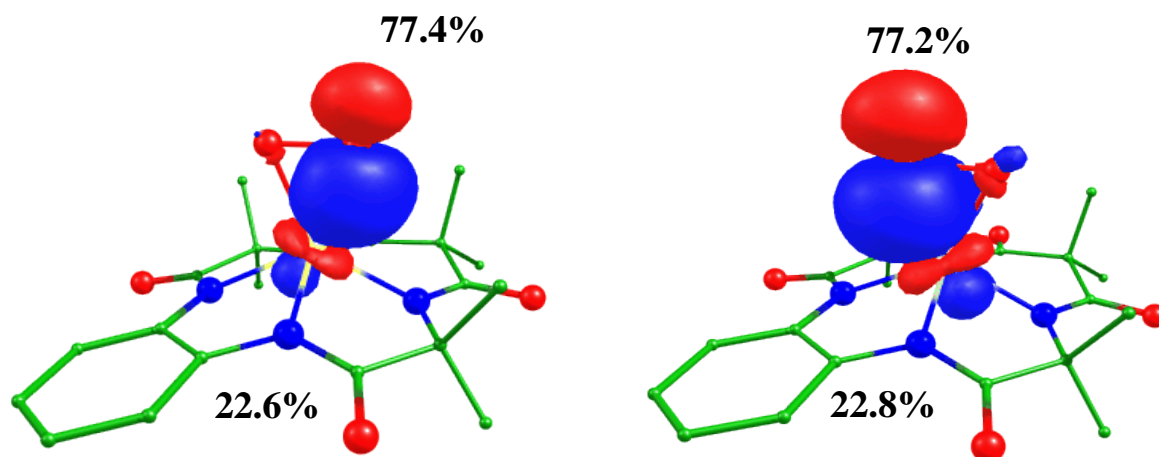
77.4% **77.2%**

22.6% **22.8%**

Figure 3.9. Computed NBO plots for species IIIb (^{6}IIIb$_{hs}$).

3.3.4 Electronic structure and energetics of hydroperoxo [(TAML)Fe^{IV}-OOH]$^.$ (species IV)

After the abstraction of hydrogen from organic substrates by superoxo/peroxo species can form hydroperoxo species. Similar to the above species, there are three possible spin states of species IV, in which intermediate spin (S=1) is found to be the ground state, and other spin states, S=2 and S=0 lie at 49.1 and 77.9 kJ/mol higher in energy, respectively. The optimized structure and spin density plot of the ground state are shown in Figure 3.10a,b. The Fe-O1 and O1-O2 bond lengths are computed to be 1.889 Å and 1.486 Å. The Fe-O1 bond length decreases while the O1-O2 bond length increases from the superoxo species II. The computed shift in the position of the iron atom is found to be 0.19 Å. The decrease in Fe-O1 bond length is due to the overlapping between d-orbital of Fe and p-orbital of the oxygen atom. The HOMO-LUMO gap also decreases to 0.059 eV compared to species II and IIIb (see Figure 3.10c). The NBO analysis shows that iron d_z^2 orbital has (20.1%) orbital contribution whereas p_z orbital of oxygen has a 79.9 % orbital contribution (see NBO plot Figure 10d). There is a reduction of spin density at the oxygen atoms also observed. The eigenvalue plot is

shown in Figure 3.5b. The electronic configuration at the metal center is found to be $(d_{xz})^2$, $(d_{yz})^1$, $(d_{xy,})^1$, $(d_z^2)^0$ and $(d_{x^2-y^2})^0$.
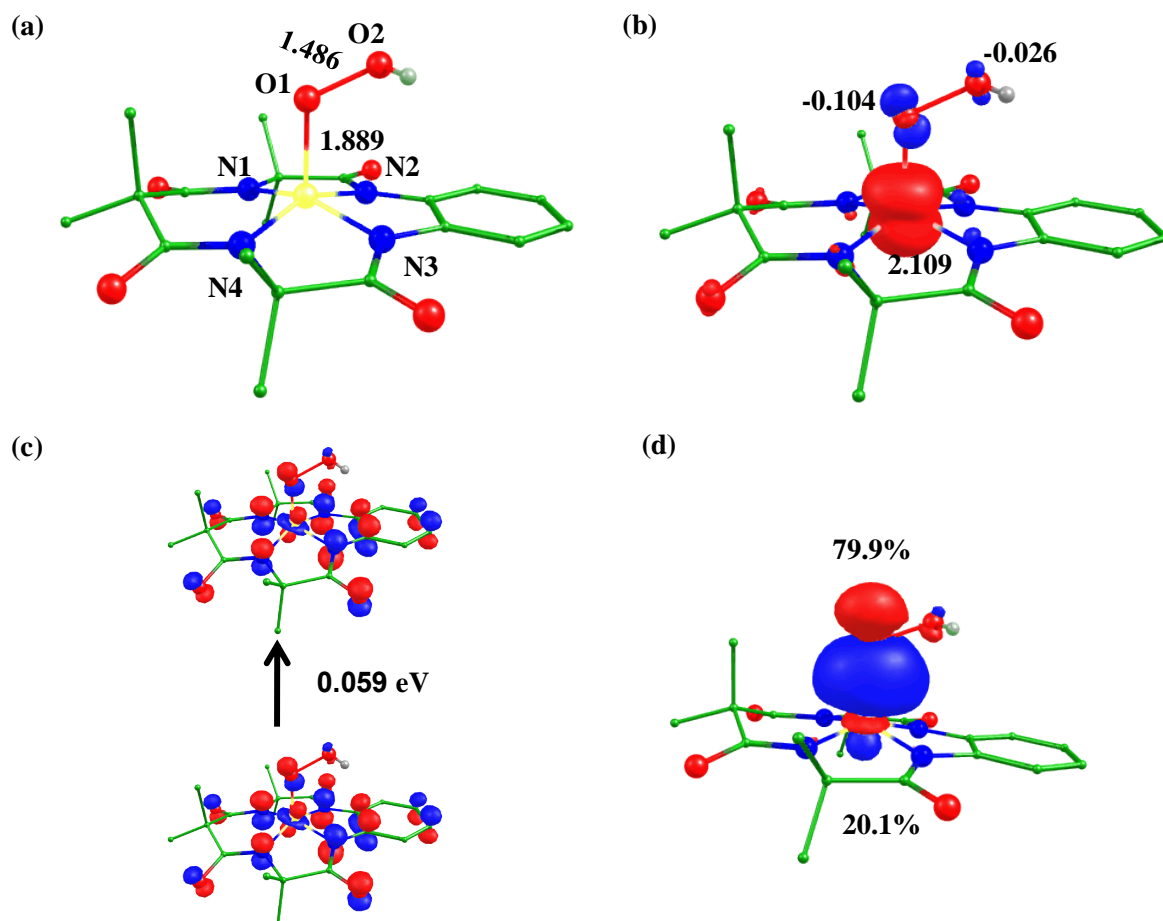
(a)

(b)

(c)

(d)

Figure 3.10. B3LYP-D2 a) optimized structure (bond length in Å) and b) its spin density plot of $^3IV_{is}$ d) Computed NBO plot of specie IV ($^3IV_{is}$).

The stretching frequency of the Fe-O and O-O bond is computed to be $v420\text{cm}^{-1}$ and $v823\text{cm}^{-1}$, decrease in O-O stretching frequency by $v373\text{cm}^{-1}$ compared to end on $[(TAML)Fe^{IV}\text{-}\eta^1\text{-}O_2]^{\bullet-}$ species supported an increase in O1-O2 bond length.

3.3.5 Electronic structure and spin energetics of $[(TAML)Fe^{IV}\text{-}O]^{2-}$ (species V)

The first direct evidence for the generation of a non-heme Fe^{IV}-O complex was reported by Wieghardt *et al.* at the start of this millennium,[99] and this is well characterized by X-ray and

spectroscopically. Non-heme Fe^{IV}-O species became a popular active oxidant that can show reactivity towards C-H, O-H, N-H, and oxygen atom transfer reactions, etc. in detail.[68-69] Here we have also optimized high (quintet, S=2), intermediate (triplet, S=1) and low spin (singlet, S=1) states of the species, and our DFT calculations reveal that the triplet state is found to be the ground state with the quintet and singlet states lie at 86.4 kJ/mol and 112.6 kJ/mol higher in energy, respectively, (see Figure 3.1) and this ground state is inconsistent with earlier experimental and theoretical reports (see Figure 3.11(a,b)). [54,65-68]
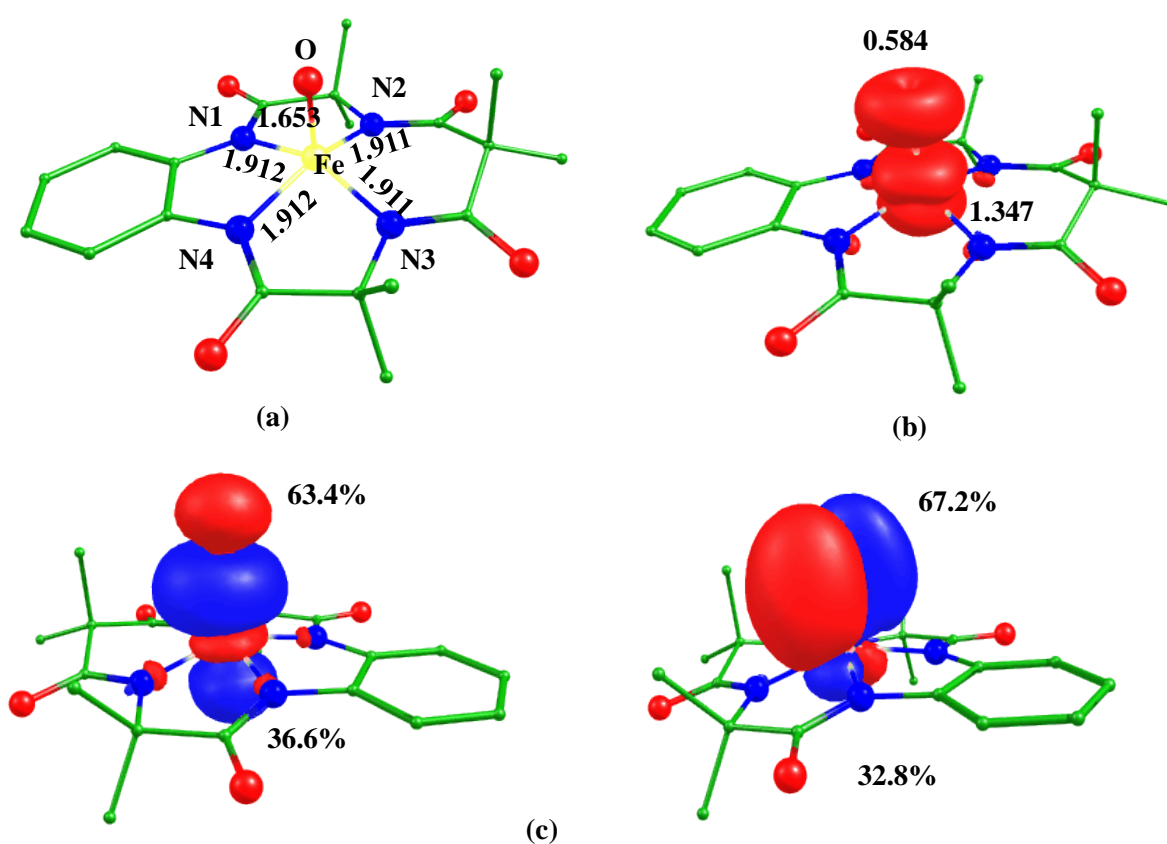

Figure 3.11. B3LYP-D2 a) optimized structure (bond length in Å), b) its spin density plot of $^3V_{is}$, and c) Computed NBO plots of $^3V_{is}$.

The calculated Fe-N_{avg} bond length is 1.929 Å, higher than the species I (see Table 3.1). The Fe-O bond length is found to be 1.653 Å, shorter than the other spin surface quintet and singlet state (see Table 3.1) and this shorter bond length is due to the formation of π bond between iron and oxygen reveals double bond character (see scheme 3.2).
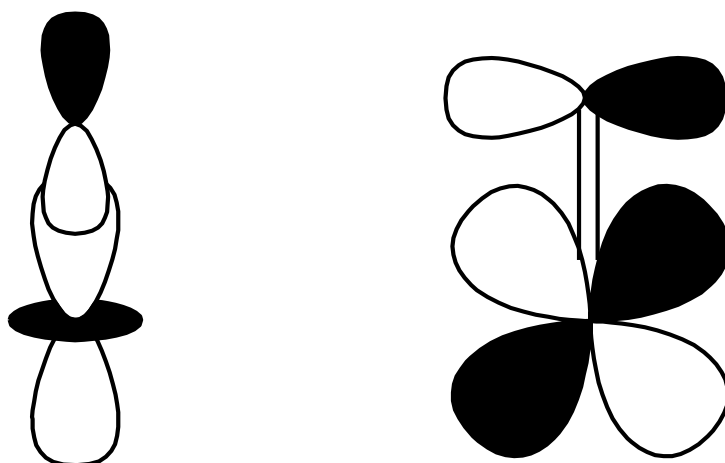
Scheme 3.2. Frontier π-orbitals of $Fe^{IV}=O$ species at $S = 3/2$ spin surface.

The Fe-O bond length matches with previous experimental and theoretical studies.[53] The orbital contribution of iron d_z^2 (36.6%) and oxygen p_z (63.4%) suggests the formation of σ-bond and also supported the formation of π-bond between d_{yz} and p-orbital of the oxygen (see Figure 3.11c). However, additional orbital contributions between iron and oxygen atoms show the formation of π-bond and unfold the presence of a double bond character between them.

The electronic configuration of the ground state is computed to be $(d_{xy})^2$, $(d_{yz})^1$, $(d_{xz,})^1$, $(d_z^2)^0$ and $(d_{x^2-y^2})^0$ (see Figure 3.12a). A similar electronic configuration is also found with other iron(IV)-oxo species.[53] Here, $d_{x^2-y^2}$ orbital has higher energy than the d_z^2 due to the strong equatorial ligand field of the TAML ligand. The stretching frequency of the Fe-O bond is found to be 880 cm^{-1} reveals the strength of the bond. The computed Fe-N$_{avg}$ bond length is found to be 1.971 Å and this is longer than the species I. The iron center of this species is also shifted towards the z-axis by 0.35 Å (see Table 3.4). The computed HOMO-LUMO gap is 3.605 eV (see Figure 3.13a).
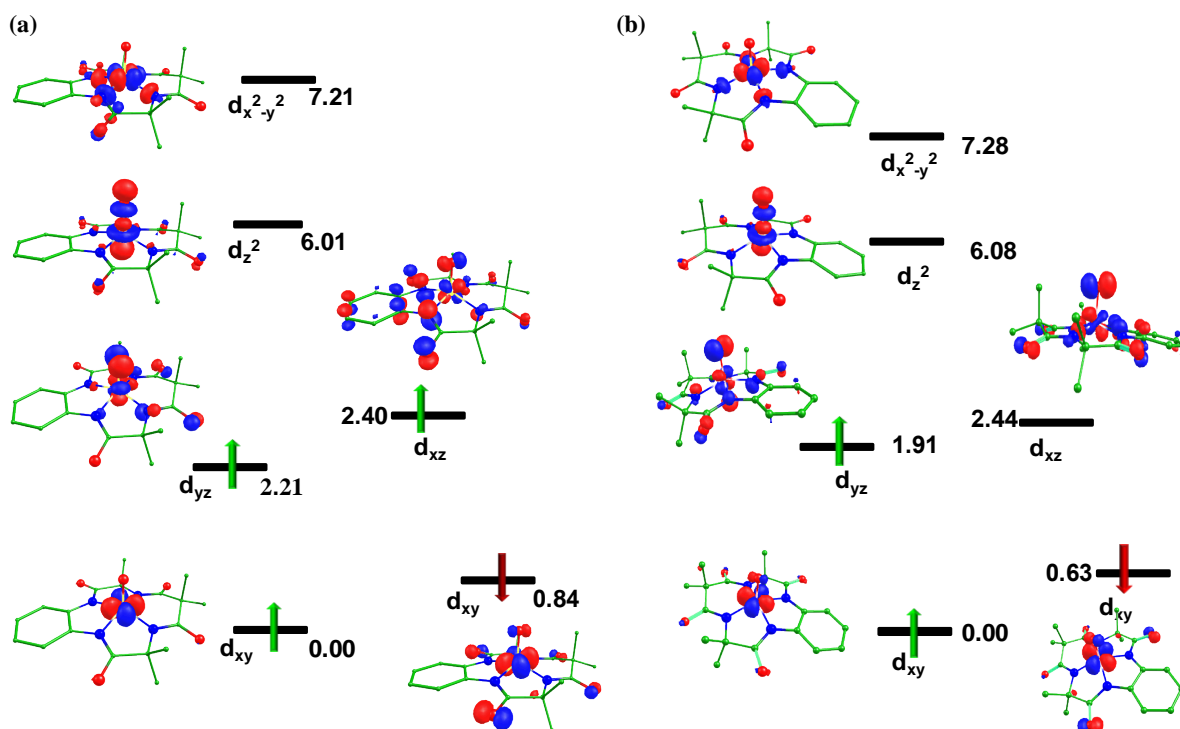
Figure 3.12. Computed eigenvalue plot incorporating energies computed for *d*-based orbitals for alpha and beta spin corresponding to the ground state a) (^{5}V$_{is}$) b) ^{2}VI (energies are given in eV).
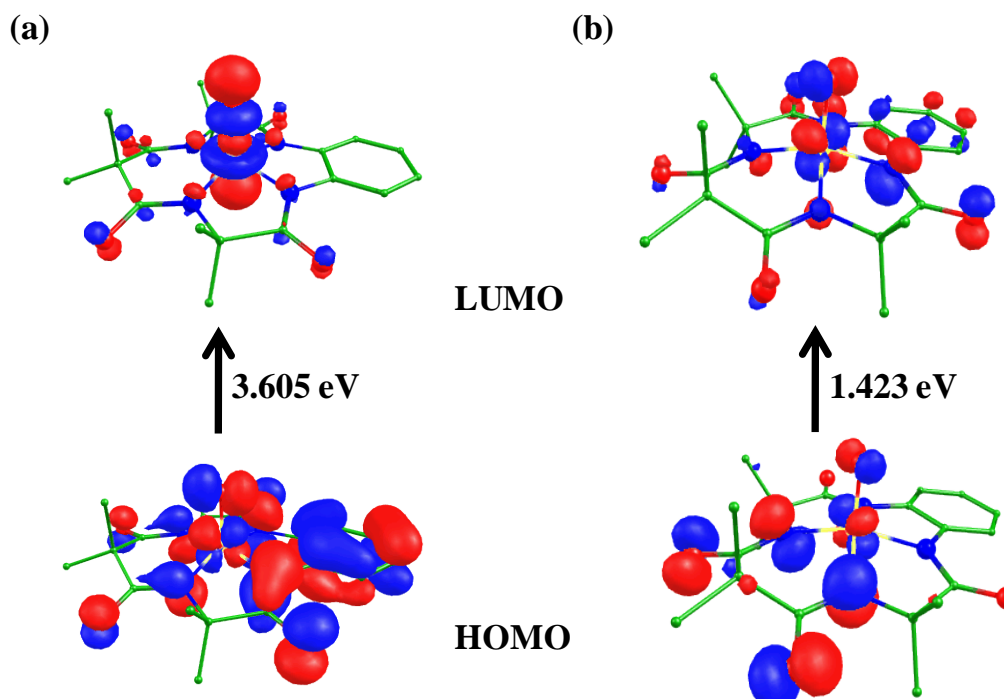

Figure 3.13. The HOMO-LUMO frontier molecular orbitals of (a) species V, and (b) species VI.

The computed spin density value of 1.347 is located at the iron center and the ferryl oxygen is also acquired spin density ($\rho = 0.584$). The coordinated nitrogen atoms also gained some spin density via electron delocalization. A significant spin density at the oxygen atom can activate the C-H/O-H bond of aliphatic/aromatic hydrocarbons.[71-74]

3.3.6 Electronic structure and spin energetics of [(TAML)Fe^V-O]$^-$ species (VI)

One electron oxidation of (species V) can produce the [(TAML)Fe^V-O]$^-$ (species VI) and this species with sufficient thermal stability for extensive spectroscopic characterization was generated by collins's.[50] Our DFT calculations show that the low spin (S=1/2; ^{2}VI) is found to be the ground state with high spin (S=3/2; ^{4}VI) lies at 5.21 kJ/mol higher in energy. The energy gap and the ground state are consistent with previous experimental and theoretical studies on similar architectures.[100]
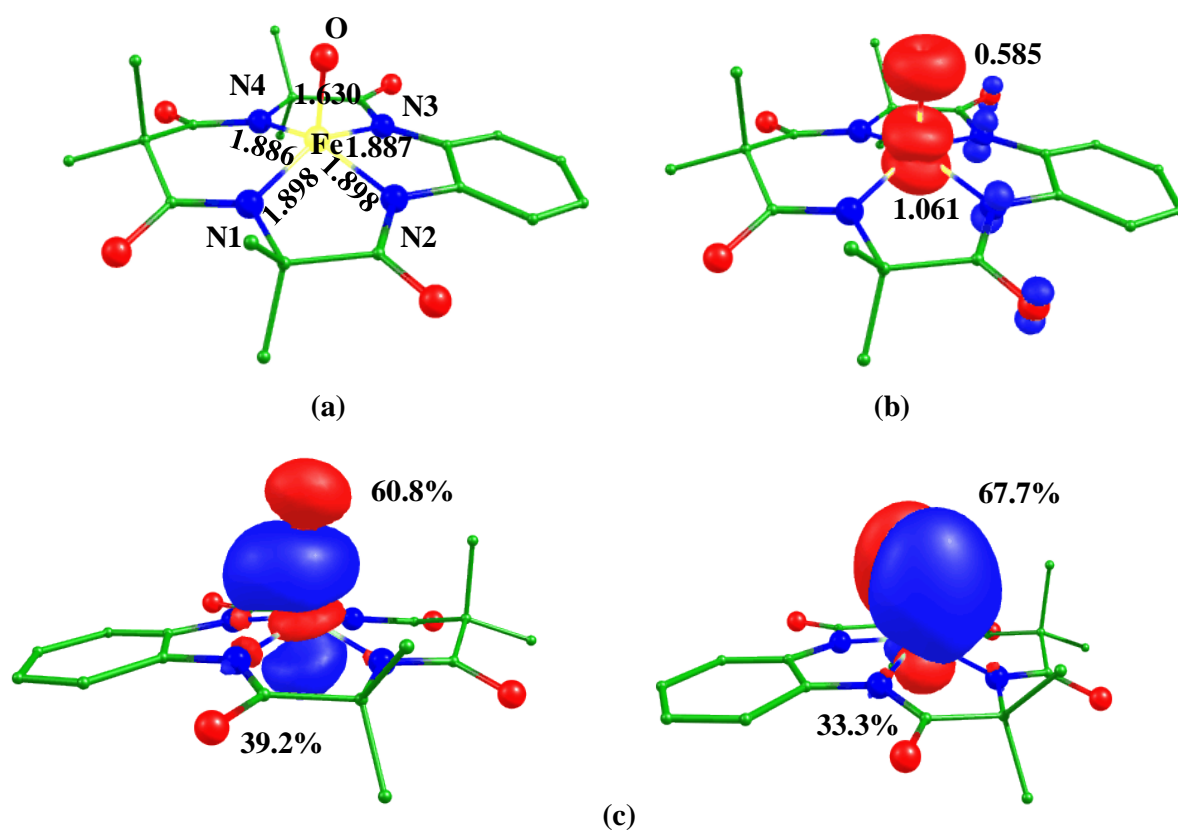

(a)

(b)

(c)

Figure 3.14. B3LYP-D2 a) optimized structure (bond length in Å), b) its spin density plot of $^3V_{is}$, and c) computed NBO plot of species VI ($^2VI_{ls}$).

Optimized structure and corresponding spin density plot of the ground state (^2VI) are shown in Figure 3.14(a,b). The Fe-O bond length of the ground state is calculated to be 1.630 Å which corresponds to a double Fe-O covalent bond character in the ground state and the bond length is slightly elongated to 1.662 Å in the high spin state. The structural parameters are also in agreement with a similar X-ray structure (see Table 3.1).[50] The increment in equatorial Fe-N bond lengths is observed when the spin state changes from low spin to high spin. If Fe^V=O species are compared with Fe^{III} species, it is revealed that the bond length of Fe-N bonds gets elongated in the case of Fe^V=O species. The eigenvalue plot along with the orbital diagram of the ground state (^2I) is shown in Figure 3.12b. For square pyramidal geometry, d_{xz} and d_{yz} are frontier orbitals while d_{xy} is the lowest-lying within the d-orbital. The electronic configuration is computed to be $(d_{xy})^2, (d_{yz})^1, (d_{xz,})^0, (d_z^2)^0$ and $(d_{x^2-y^2})^0$ (see Figure 3.12b). The spin density value of 1.061 has been detected on the Fe center inferring the presence of one unpaired electron. Similarly, all the nitrogen atoms also gain electron density via spin delocalization. Spin densities on the iron and oxygen are of the same signs while nitrogen atoms acquire opposite signs which indicate that the spin of the electrons is the same on iron and oxygen while it is opposite on the nitrogen atoms. The computed Fe-O bond length is found to be smaller than the species V (see Table 3.1) and this is due to the increment in the double bond character between the iron center and oxygen atom. The computed HOMO-LUMO gap is 1.423 eV smaller than species V (see Figure 3.13b). The shift in the position of the iron atom is computed to be 0.40 Å. The redox potential change upon the oxidation at the iron center can also increase the reactivity of species (VI).[71,101] From the NBO calculations, we see that iron d_z^2 (39.2%) which is greater than species VI and oxygen p_z (60.8%) suggests a stronger bond between iron and oxygen than species V (see Figure 3.14c). A spin density at

the oxygen can help in C-H/O-H bond activation as well as in olefin epoxidation/sulfoxidation.[50,102]

3.3.7 Electronic structure and energetics of [(TAML)Fe^{IV}-μO-(TAML)Fe^{IV}]$^{2-}$ (species VII)

The well-characterized [(TAML)Fe^{V}-O]$^{-}$ species can react with [Fe^{III}(TAML)]$^{-}$ species I to generate μ-oxo dinuclear derivative [(TAML)Fe^{IV}-μO-Fe^{IV}(TAML)]$^{2-}$ (species VII).[50,53] This μ-oxo bridged dinuclear species is also well characterized in previous studies.[55] The dimer [(TAML)Fe^{IV}-μO-Fe^{IV}(TAML)]$^{2-}$ (species VII) possesses the same ligand, one can assume that both the iron centers are likely to have an identical spin on both the iron centers. There are five possible spin states such as ^{9}VII$_{hs}$, ^{1}VII$_{hs}$, ^{5}VII$_{is}$, ^{1}VII$_{is,}$ and ^{1}VII$_{ls}$ for species VII, and the schematically electronic interactions for each of the iron centers are shown in Table 3.5.

Table 3.5. Possible spin states of [(TAML)Fe^{IV}-μO-Fe^{IV}(TAML)]$^{2-}$ species.

	Electronic configuration		
Spin state	**Fe(IV)**	**Fe(IV)**	**Relative energy(kJ/mol)**
^{9}VII$_{hs}$	$\pi^*_{xz}\uparrow \pi^*_{yz}\uparrow \delta_{xy}\uparrow \sigma^*_z{}^2\uparrow \delta_{x^2-y^2}{}^2$	$\pi^*_{xz}\uparrow \pi^*_{yz}\uparrow \delta_{xy}\uparrow \sigma^*_z{}^2\uparrow \delta_{x^2-y^2}{}^2$	68.8
^{1}VII$_{hs}$	$\pi^*_{xz}\uparrow \pi^*_{yz}\uparrow \delta_{xy}\uparrow \sigma^*_z{}^2\uparrow \delta_{x^2-y^2}{}^2$	$\pi^*_{xz}\downarrow \pi^*_{yz}\downarrow \delta_{xy}\downarrow \sigma^*_z{}^2\downarrow \delta_{x^2-y^2}{}^2$	82.4
^{5}VII$_{is}$	$\pi^*_{xz}\uparrow\downarrow \pi^*_{yz}\uparrow \delta_{xy}\uparrow \sigma^*_z{}^2 \delta_{x^2-y^2}{}^2$	$\pi^*_{xz}\uparrow\downarrow \pi^*_{yz}\uparrow \delta_{xy}\uparrow \sigma^*_z{}^2 \delta_{x^2-y^2}{}^2$	3.3
^{1}VII$_{is}$	$\pi^*_{xz}\uparrow\downarrow \pi^*_{yz}\uparrow \delta_{xy}\uparrow \sigma^*_z{}^2 \delta_{x^2-y^2}{}^2$	$\pi^*_{xz}\uparrow\downarrow \pi^*_{yz}\downarrow \delta_{xy}\downarrow \sigma^*_z{}^2 \delta_{x^2-y^2}{}^2$	0
^{1}VII$_{ls}$	$\pi^*_{xz}\uparrow\downarrow \pi^*_{yz}\uparrow\downarrow \delta_{xy} \sigma^*_z{}^2 \delta_{x^2-y^2}{}^2$	$\pi^*_{xz}\uparrow\downarrow \pi^*_{yz}\uparrow\downarrow \delta_{xy} \sigma^*_z{}^2 \delta_{x^2-y^2}{}^2$	186.1

We have optimized all five spin surfaces of species VII, and our DFT calculations predicted that the intermediate spin state (^{1}VII$_{is}$) with antiferromagnetic coupling between both the iron centers is found to be the ground state and other spin surfaces such as ^{9}VII$_{hs}$, ^{1}VII$_{hs}$, ^{5}VII$_{is}$,

and $^1VII_{ls}$ lie at 68.8, 82.4, 3.3, 186.1 kJ/mol higher in energy, respectively. This ground state is also supported by experimental observation.[55] The optimized structure and spin density plot of the ground state ($^1VII_{is}$), and $^5VII_{is}$ are shown in Figure 3.15. The Fe1/Fe2-N_{avg} bond lengths are found to be 1.913 Å and 1.895 Å which are greater than species I and these are also in agreement with the experimental data.[55] The bond angle of Fe-O-Fe is found to be 160.5° and this bending around bridged oxygen atom is aroused due to the ligated nitrogen atom donates the electron density to the empty d_z^2 which overlap to the p-orbital of the oxygen atom, and this also includes the double bond formation between iron and oxygen atoms.
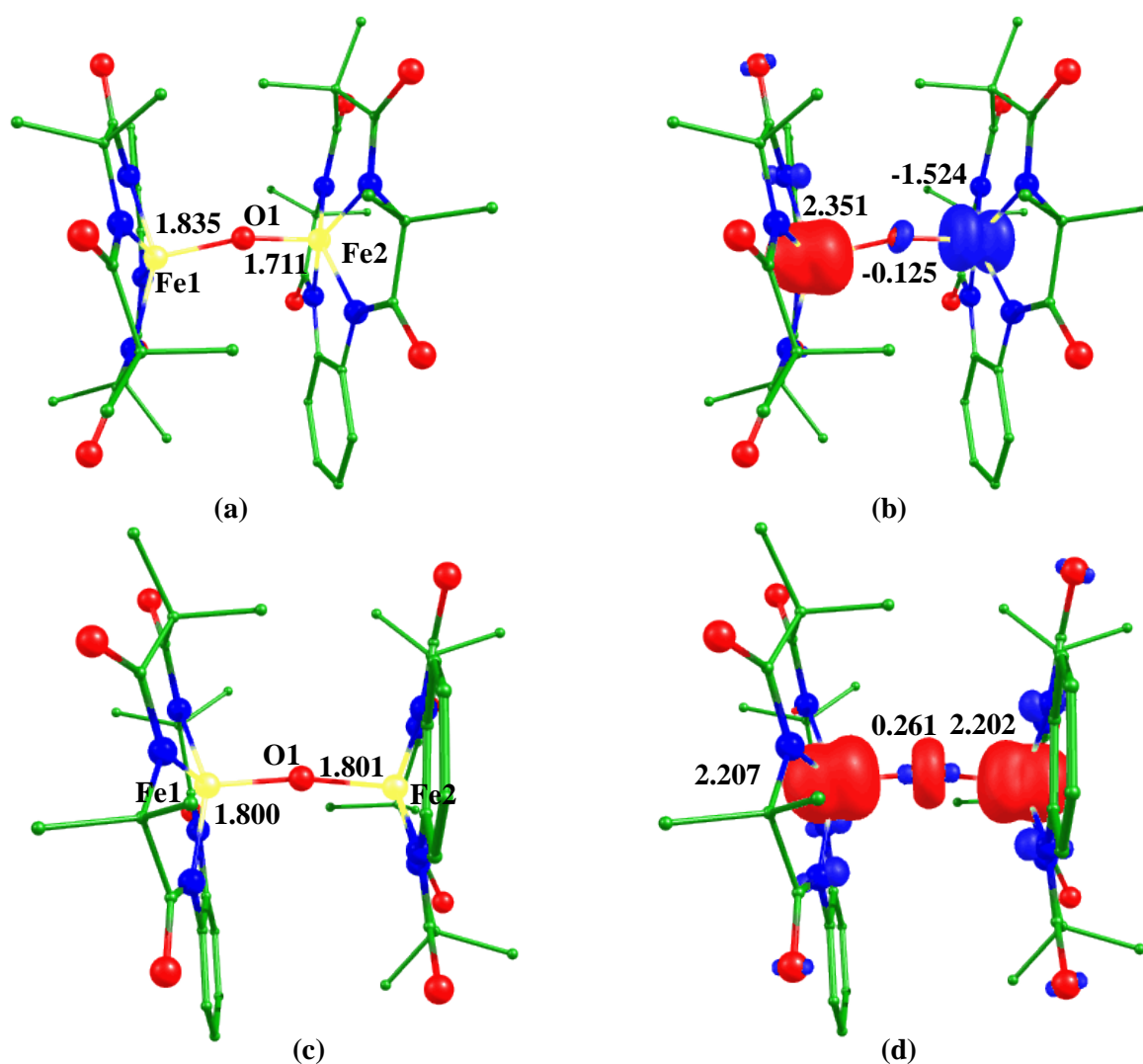

Figure 3.15. B3LYP-D2 a) optimized structure (bond length in Å) of $^1VII_{is}$ and its b) spin density plot, c) optimized structure (bond length in Å) and d) its spin density plot of $^5VII_{is.}$

Our calculations also reveal that both the iron centers have equivalent formal charges, but there is a significant difference in Fe-O bond lengths. Computed Fe1-μ-oxo and Fe2-μ-oxo bond distances are found to be 1.835 Å and 1.711 Å, respectively, and these are also observed on similar structures in previous reports.[73] Selected bond lengths and spin density values are shown in Table 3.1 and Table 3.2. The iron atom (Fe2) possess beta electron (the negative spin density in Figure 3.15b) has a shorter Fe-O bond length compared to the other Fe atom. Spin density on both the iron centers is found to be 2.351 and -1.524. There is also a significant electron density found at the oxygen atom.
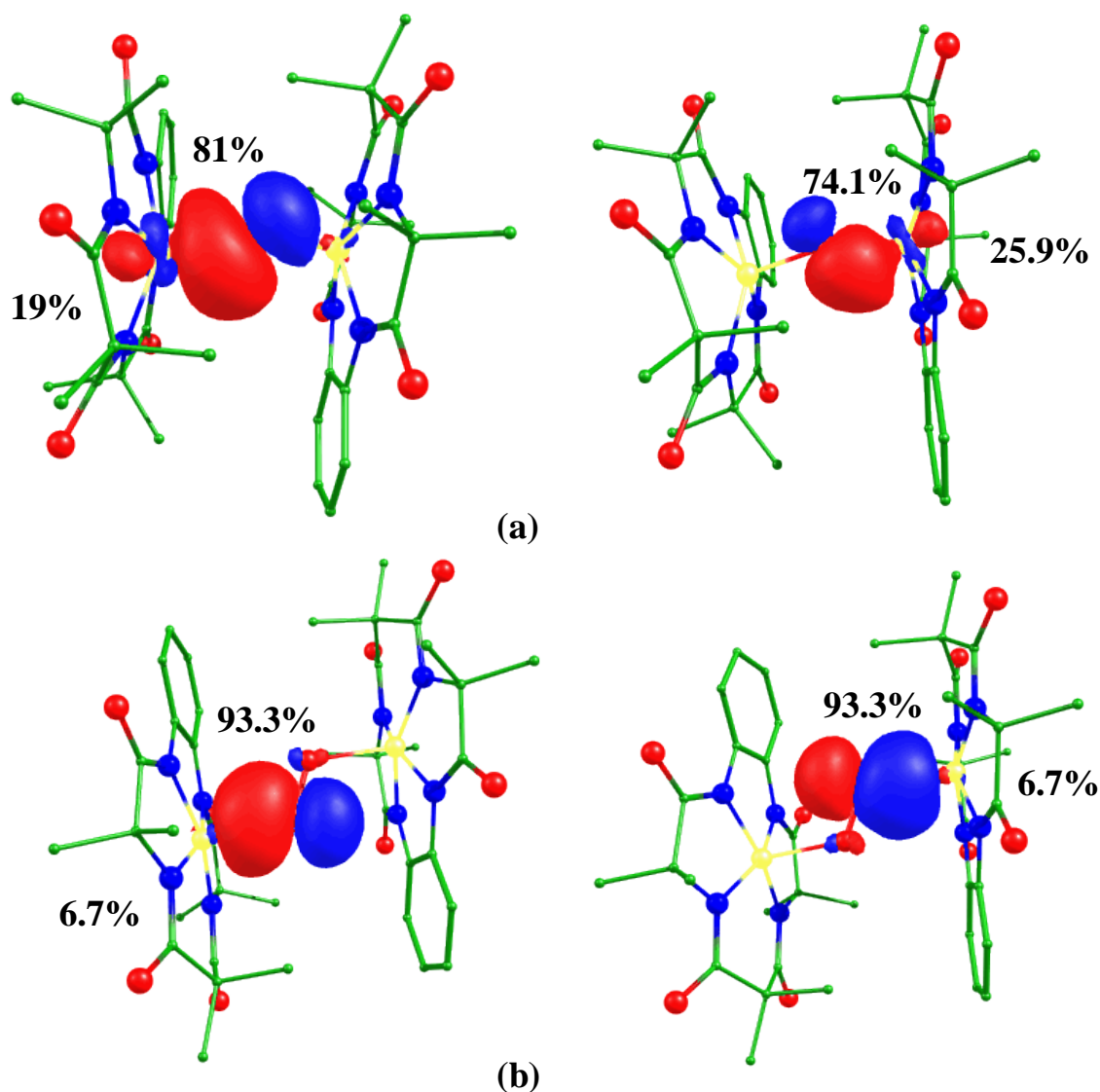

Figure 3.16. Computed NBO plots of the ground state of a) species VII, and b) species VIII.

From the NBO analysis, σ bonding effects also observed between the iron Fe1 (19%) and μ-oxo (81%) whereas the Fe2-μ-oxo possesses the additional π-bond character as the Fe2 (25.9%) and μ-oxo (74.1%) orbital contribution is detected (see Figure 3.16a). From the earlier report, di-μ-oxo-diiron(VII) species, two μ-oxo groups yield a symmetric Fe(IV)-oxo environment.[103] Here, our calculations suggest an asymmetric environment with one shorter and other longer Fe-O bond lengths due to the presence of one μ-oxo group.[73] The Fe-Fe bond distance is 3.495 Å. From Table 3.4, we see that the displacements along z-axis are -0.41 Å and 0.42 Å and these opposite sign indicates that both iron centers are approaching each other.
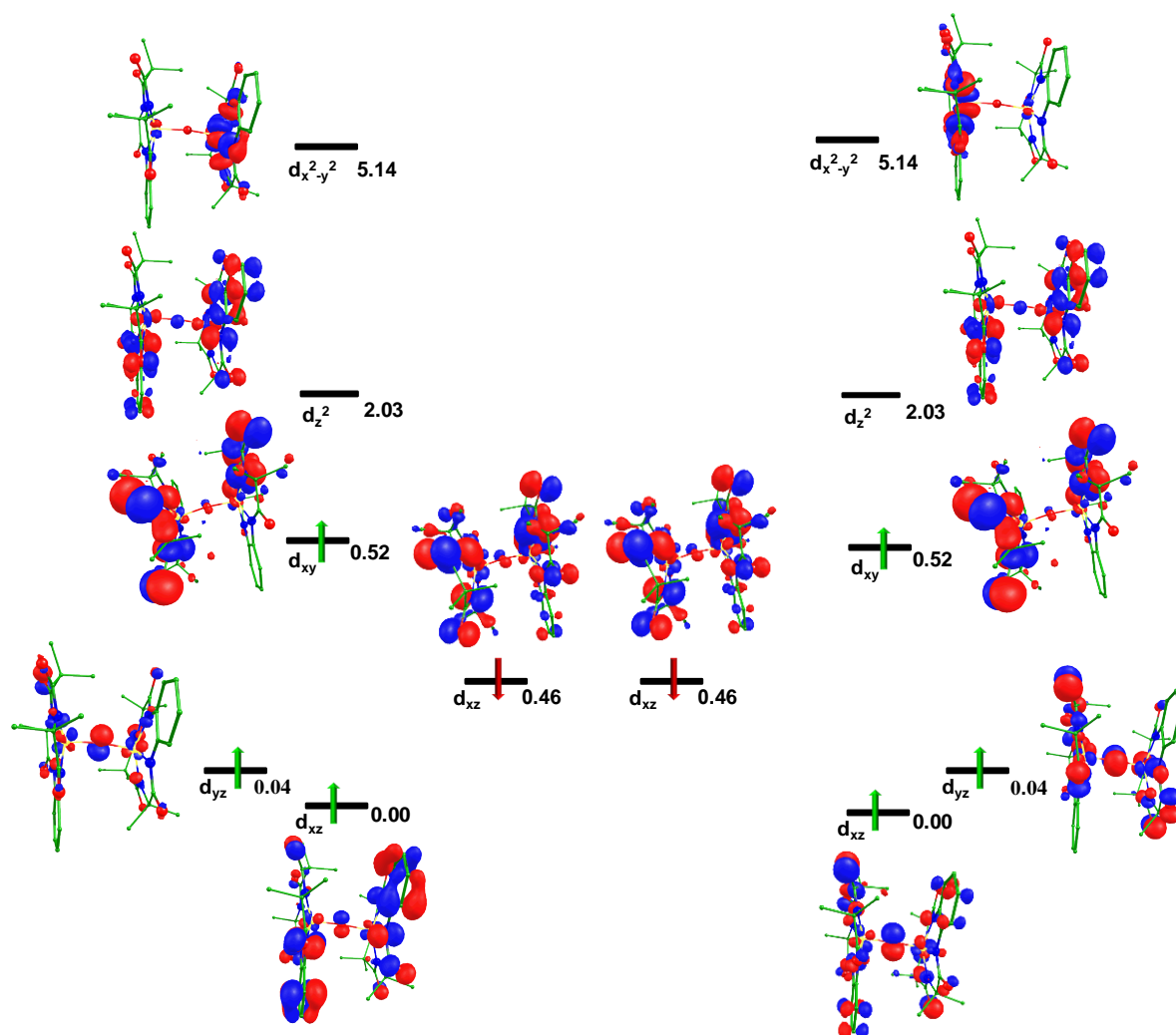

Figure 3.17. Computed Eigen-value plot incorporating energies computed for *d*-based orbitals for alpha and beta spin corresponding to the ground state (^{1}VII$_{is}$) (energies are given in eV).

Nitrogen atoms coordinated to iron atoms gain significant electron density via the electron delocalization mechanism. The bridged oxygen atom possesses a significant electron density that can help in C-H/O-H bond activation.[72-73] The eigenvalue plot is shown in Figure 3.17, and both the Fe atoms have the similar electronic configuration of $(d_{xy})^2$, $(d_{yz})^1$, $(d_{xz})^1$, $(d_z^2)^{0,}$ and $(d_{x^2-y^2})^0$ with alpha electrons in d_{xz} and d_{yz} at Fe1 center and beta electrons in d_{xz} and d_{yz} at Fe2 center (see Figure 3.17.) The d_z^2 and $d_{x^2-y^2}$ are unoccupied due to much higher in energy. The HOMO-LUMO gap is found to be 0.939 eV (see Figure 3.18a). The computed magnetic exchange coupling constant is found to be J = -88.82 cm^{-1} and this shows that antiferromagnetic coupling occurs between both the iron centers.
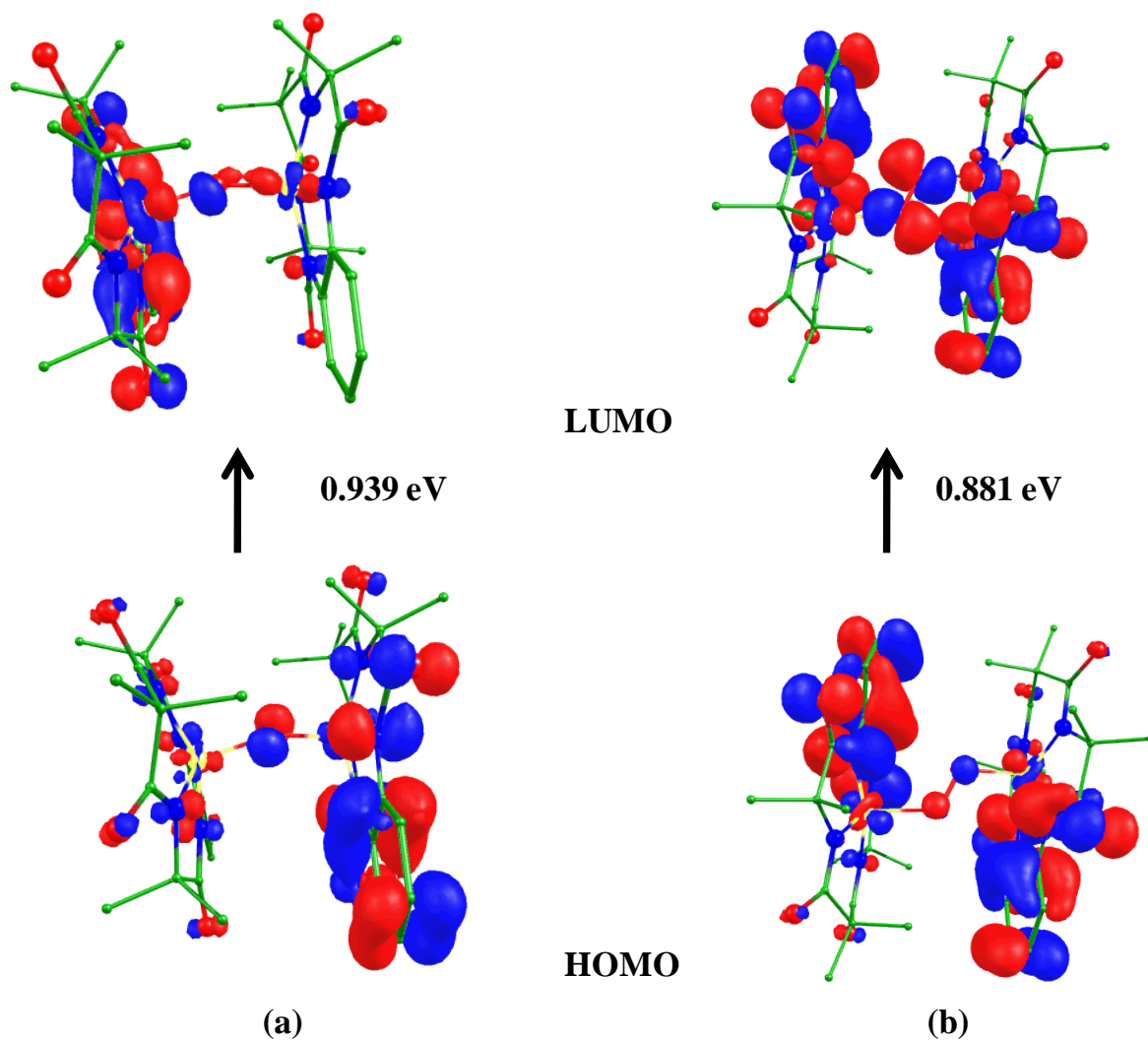

Figure 3.18. The HOMO-LUMO frontier molecular orbitals of species VII (^{1}VII$_{is}$) and species VIII (^{5}VIII$_{is}$).

The stretching frequency for Fe1-μO and Fe2-μO are υ 349 cm^{-1} and υ 766 cm^{-1} respectively, these frequencies are supported by the iron-μ-oxo bond distances.

3.3.8. Electronic structure and spin energetics of [(TAML)Fe^{IV}-O-O-Fe^{IV}(TAML)]$^{2-}$ (species VIII)

When they react in 1:2 of species I and dioxygen can generate oxygen bridged dinuclear (μ-1,2-peroxo) species; [(TAML)Fe^{IV}-O-O-Fe^{IV}(TAML)]$^{2-}$ (species VIII).[55] Similar to species VII, we have also optimized five possible spin states of species VIII (see Table 3.6) and our DFT calculations show that the ^{5}VIII$_{is}$ spin state is the ground state with ^{9}VIII$_{hs}$, ^{1}VIII$_{hs,}$ ^{1}VIII$_{is}$ and ^{1}VIII$_{ls}$ lie at 36.2, 13.0, 12.9, and 356.3 kJ/mol higher in energy, respectively. The optimized structure and spin density plot of the ^{5}VIII$_{is}$ (ground state) and the corresponding spin state (^{1}VIII$_{is}$) are shown in Figure 3.19.

Table 3.6 Possible electronic configuration for [(TAML)Fe^{IV}-O-O-Fe^{IV}(TAML)]$^{2-}$ species VIII.

Spin state	Electronic configuration		Relative energy(kJ/mol)
	Fe(IV)	Fe(IV)	
^{9}VIII$_{hs}$	$\pi^*_{xz}\uparrow \pi^*_{yz}\uparrow \delta_{xy}\uparrow \sigma^*_{z^2}\uparrow \delta_{x^2-y^2}$	$\pi^*_{xz}\uparrow \pi^*_{yz}\uparrow \delta_{xy}\uparrow \sigma^*_{z^2}\uparrow \delta_{x^2-y^2}$	36.2
^{1}VIII$_{hs}$	$\pi^*_{xz}\uparrow \pi^*_{yz}\uparrow \delta_{xy}\uparrow \sigma^*_{z^2}\uparrow \delta_{x^2-y^2}$	$\pi^*_{xz}\downarrow \pi^*_{yz}\downarrow \delta_{xy}\downarrow \sigma^*_{z^2}\downarrow \delta_{x^2-y^2}$	13.0
^{5}VIII$_{is}$	$\pi^*_{xz}\uparrow\downarrow \pi^*_{yz}\uparrow \delta_{xy}\uparrow \sigma^*_{z^2} \delta_{x^2-y^2}$	$\pi^*_{xz}\uparrow\downarrow \pi^*_{yz}\uparrow \delta_{xy}\uparrow \sigma^*_{z^2} \delta_{x^2-y^2}$	0
^{5}VIII$_{is}$	$\pi^*_{xz}\uparrow\downarrow \pi^*_{yz}\uparrow \delta_{xy}\uparrow \sigma^*_{z^2} \delta_{x^2-y^2}$	$\pi^*_{xz}\uparrow\downarrow \pi^*_{yz}\downarrow \delta_{xy}\downarrow \sigma^*_{z^2} \delta_{x^2-y^2}$	12.9
^{1}VIII$_{ls}$	$\pi^*_{xz}\uparrow\downarrow \pi^*_{yz}\uparrow\downarrow \delta_{xy} \sigma^*_{z^2} \delta_{x^2-y^2}$	$\pi^*_{xz}\uparrow\downarrow \pi^*_{yz}\uparrow\downarrow \delta_{xy} \sigma^*_{z^2} \delta_{x^2-y^2}$	356.3

The calculated Fe1-μO1 and Fe2-μO2 bond lengths of the ^{5}VIII$_{is}$ state are found to be 2.124 Å and 2.127 Å, respectively, and are higher than the corresponding bond lengths of species ^{I}VII$_{is}$. The O1-O2 bond length is 1.334 Å, in agreement with the other μ-1,2-peroxo

species,[104] and the computed stretching frequency for the O-O bond is $\nu 1050$ cm^{-1} corresponds to the formation of peroxo linkage.
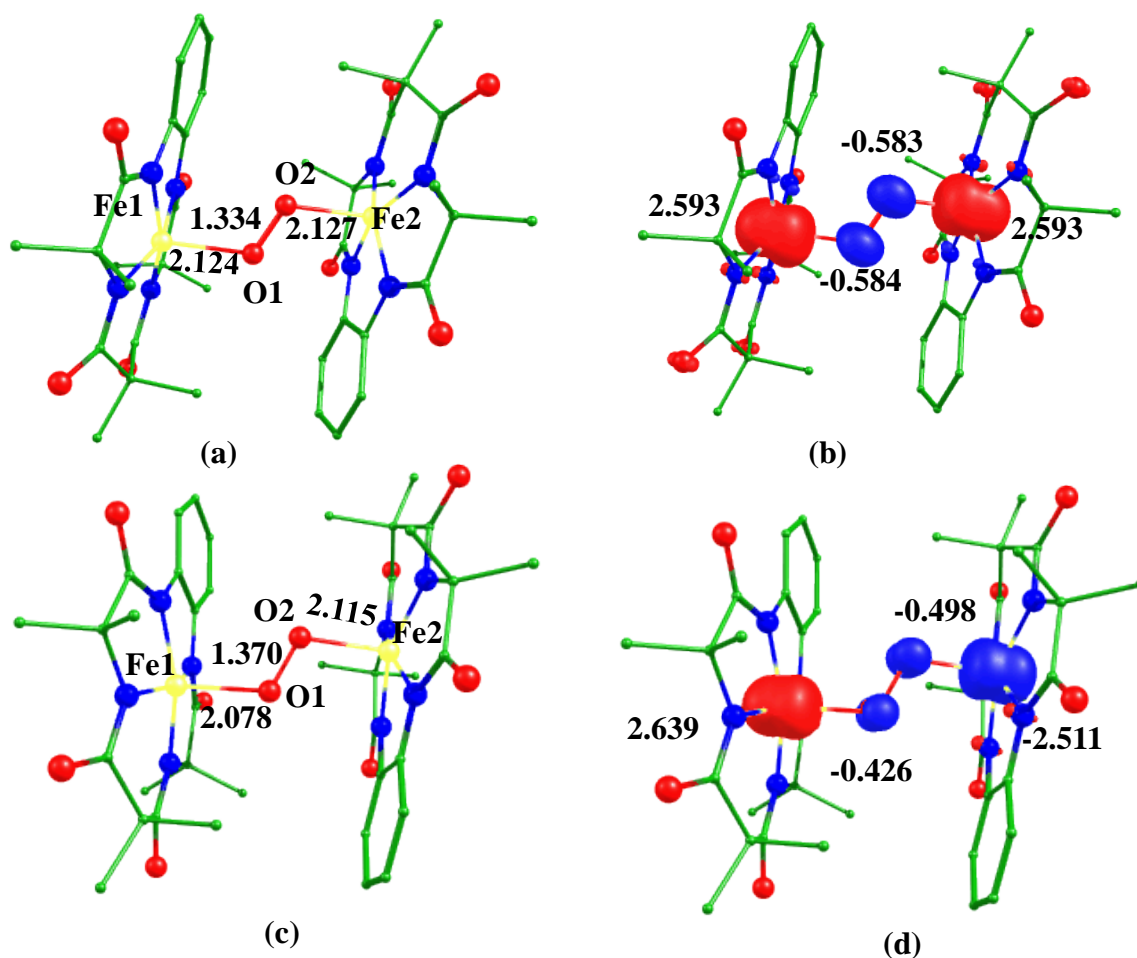

Figure 3.19. B3LYP-D2 a) optimized structure (bond length in Å) and b) its spin density plot of $^5VIII_{is,}$ c) optimized structure (bond length in Å) and d) its spin density plot of $^1VIII_{is}$.

The same stretching frequencies ($\nu 258$cm^{-1}) are found for both Fe1-O1 and Fe2-O2 bonds, smaller than the μ-oxo bridge species, indicates that Fe-O bond length is longer in (μ-1,2-peroxo) species and suggested the presence of a single bond between both the iron-oxygen bonds (see Table 3.1). The Fe1-N$_{avg}$ and Fe2-N$_{avg}$ bond distances are computed to be 1.882 Å and 1.883 Å, respectively. The spin density plot of the ground state shows that both the iron centers possess the same sign of spin density suggests the presence of ferromagnetic coupling between iron centers and this is also supported by the estimation of the magnetic exchange

with the value of 777.44 cm^{-1}. Although the experimental magnetic exchange value of the species is not observed yet. The coordinated nitrogen atoms to the iron center also acquired electron density due to electron delocalization.
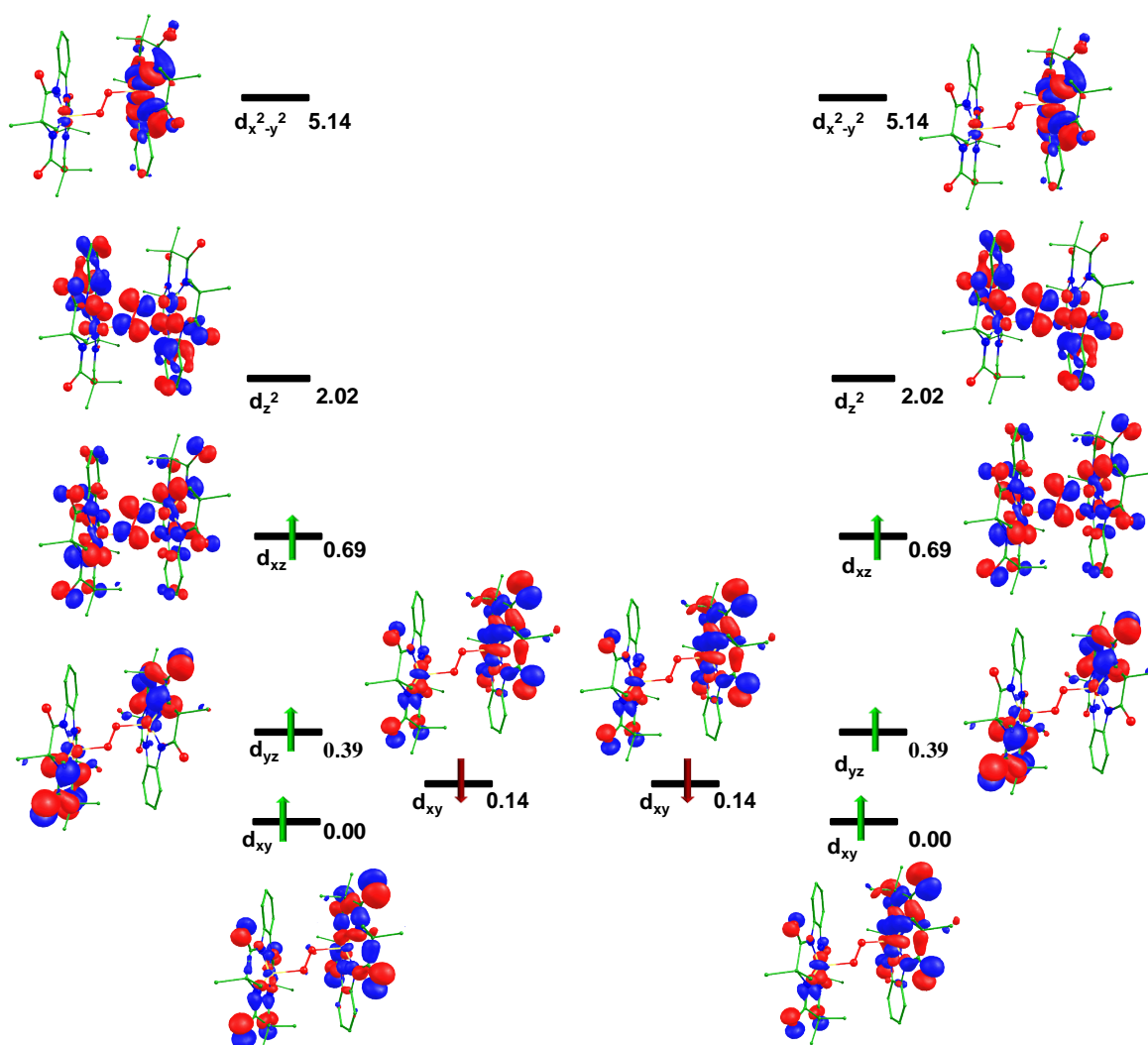
Figure 3.20. Computed Eigen-value plot incorporating energies computed for *d*-based orbitals for alpha and beta spin corresponding to the ground state (^{5}VIII$_{is}$) (energies are given in eV).

The computed HOMO-LUMO gap is 0.881 eV smaller than species VII (see Figure 3.18b). Similar to species VII, here also, displacements along the z-axis have an opposite sign is 0.04 Å and -0.07 Å, indicating that both iron centers are approaching towards each other, this displacement is smaller as compared to species VII. The eigenvalue plot also describes the

electronic configurations around both the iron centers (see Figure 3.20). It is also found that orbitals of both the Fe atoms are found to be at the same energy levels, and the electronic configuration is found to be $(d_{xy})^2$, $(d_{yz})^1$, $(d_{xz})^1$, $(d_z^2)^0$ and $(d_{x^2-y^2}^2)^0$. The d_z^2 and $d_{x^2-y^2}^2$ are unoccupied due to much higher energy. The cleavage of the peroxo linkage can generate the $[(TAML)Fe^{IV}-O]^{2-}$ species V and $[(TAML)Fe^{V}-O]^{-}$ species VI. Significant electron densities are also located at both the bridged oxygen atoms that can activate the C-H and O-H bond of the $[(TAML)Fe^{IV}-O]^{2-}$ species V and $[(TAML)Fe^{V}-O]^{-}$ species VI.

Significant electron densities are also located at both the bridged oxygen atoms can activate the C-H and O-H bond of aliphatic and aromatic compounds.[71,73,99] NBO analysis shows that Fe1-p_y 6.7% and 93.3% of O-p_x and Fe2-p_y 6.7% and 93.3% of O-p_x (see Figure 3.16b). The contribution of the iron orbital is small as compared to μ-oxo bridged complexes iron atom and this may be due to the longer bond length and also the absence of π-bond between Fe1/2-μO1/2 as compared to Fe1-O1 and Fe2-O1 of μ-oxo bridged species.

3.3.9 Comparative study

Species formed after the reactions depend upon the binding modes of dioxygen either η^1 (end-on species) or η^2 (side-on species). Here species I-VI are mononuclear whereas species VII-VIII are bridged dinuclear. Our computed parameters also show that the Fe1-O1 bond distance of species II (2.173 Å) is longer than species III (1.994 Å), whereas the O1-O2 bond length of species II (1.321 Å) is smaller than species III (1.537 Å) due to both the oxygen atoms coordinated to iron center in species III, and these are also supported by computed stretching frequencies. The shifting of the iron center of species II (0.08 Å) out of the plane is found to be smaller than species III (0.72 Å), due to repulsion between charges of both the oxygen atoms coordinated that forces the iron atom out of the plane is comparatively more in species III. The HOMO-LUMO gap of species II (1.524 eV) is computed to be smaller than

Chapter 3

species III (3.698 eV). The Fe-O1 bond distance of species IV (1.889 Å) is smaller than species II (2.173 Å) and species III (1.994 Å) may be due to protonation at the distal oxygen atom (-OOH). The HOMO-LUMO gap in species IV (0.059 eV) is smaller than species II and species III. The shift of the iron atom out of the plane in species V (0.19 Å) is larger than species II (0.08 Å) but smaller than species III (0.72 eV). In species V, the Fe-N_{avg} (1.911 Å) and Fe-O (1.653 Å) bond lengths are longer than species VI (1.892 Å and 1.630 Å for Fe-N_{avg} and Fe-O). The shift of the iron atom out of the plane in species VI (0.40Å) is calculated to be larger than the species V (0.35Å) and this may be due to the reflection of a higher charge at the iron center. HOMO-LUMO gap of species V (3.605 eV) is larger than species VI (1.423 eV) indicates higher reactivity of species VI which is also observed in previous reports.[71,53,105-106] From, the NBO analysis of species V and species VI, we have observed that both the species V and species VI have double bond character, In species VI iron atom has 39.2 % contribution which is slightly greater than species V (36.6 %) indicates that the Fe-O bond has more double bond character in species VI than species V.

In dinuclear species, VII and VIII, the Fe1/Fe2-N_{avg} computed bond distances (1.913 Å, 1.895 Å) are longer than the corresponding bond (1.882 Å, 1.883 Å) of species VIII, but iron-μ-oxo bond lengths (1.835 Å and 1.777 Å) of species VII are longer than iron-oxygen bonds (2.124 Å and 2.127 Å) of species VIII, and these are also supported by the computed stretching frequencies. From the NBO analysis of species VII, we have found that the orbital contribution of 19 % at Fe1 and 25.9 % at Fe2 center indicate that Fe2-O1 has a double bond contribution which is also supported by smaller bond Fe2-O1 bond distance.

 NBO analysis for species VIII has a small contribution at iron centers (6.7 %) to support the longer Fe1-O1 and Fe2-O2 bond lengths. The shift of the iron atom out of plane along the bridged oxygen (axial ligand) of species VII (-0.41 Å/ 0.42 Å for Fe1/Fe2) are longer than the species VIII (0.04 Å/-0.07) Å for Fe1/Fe2. HOMO-LUMO gap of species VII (0.939 eV) is

larger than species VIII (0.881 eV). Both the Iron center in species VII is antiferromagnetically coupled, while in species VIII both iron centers are ferromagnetically coupled. The HOMO-LUMO gap in binuclear species is relatively smaller than mononuclear species except for species IV.

3.4. Conclusions

Tetraamido macrocyclic ligand coordinated iron species are of great interest because of their wide role in catalytic reactions and they mimic properties of metalloenzymes. Here, we have undertaken the DFT study on mononuclear and dinuclear iron-TAML species for analyzing structures, bonding, energetics, and magnetic interactions. Some salient conclusions derived from this work is highlighted below,

(i) Our computed DFT energies using dispersion corrected hybrid B3LYP-D2 functional predicted that the intermediate spin state for $[Fe^{III}(TAML)]^-$ (species I), $[(TAML)Fe^{IV}-\eta^1-O_2]^{\bullet-}$ (species II), $[(TAML)Fe^{IV}-OOH]^-$ (species IV), $[(TAML)Fe^{IV}-O]^{2-}$ (species V), $[(TAML)Fe^V-O]^-$ (species VI), $[(TAML)Fe^{IV}-\mu O-(TAML)Fe^{IV}]^{2-}$ (species VII) and $[(TAML)Fe^{IV}-\mu O_2-Fe^{IV}(TAML)]^{2-}$ (species VIII); high spin state for $[(TAML)Fe^{III}-\eta^1-O_2]^{3-}$ (species IIIa); and low spin state for $[(TAML)Fe^V-O]^-$ species (VI) are computed as the ground state. These ground states are in good agreement with the available experimental species.[39,53,55,56]

(ii) Our computed, DFT results also show that antiferromagnetic coupling between both iron centers is found to be in μ-oxo bridge species VII whereas ferromagnetic coupling is in μ-(1,2-peroxo) species VIII.

(iii) Here, we have also observed that the computed $Fe-N_{avg}$ bond length of species I, is smaller than the rest of the studied species II-VIII.

(iv) The increase in the oxidation state increases the bond strength confirmed by decrease in bond length and increase in stretching frequency.

(v) The iron atom gets out of the plane on reaction with dioxygen, the shift in the position of the iron atom along the z-axis of the mononuclear species are computed to be, 0.08 Å (species II), 0.72 Å (species III), 0.19 Å (species IV), 0.35 Å (species V) and 0.40 Å (species VI), and in the dinuclear species, -0.41 Å/ 0.42 Å for Fe1/Fe2 (species VII) and 0.04 Å/-0.07 Å for Fe1/Fe2 (species VIII).

(vi) NBO analysis, orbital contributions of iron and oxygen, and iron atoms explained the ionic and the covalent nature of metal-oxygen bond along with the formation of π-bond.

(vii) The nitrogen atom coordinated to the iron atom gains electrons density via the electron delocalization mechanism. The significant spin density at the oxygen atom can be a witness for C-H/O-H/N-H bond activation.

To this end, these findings have direct relevance to the community working in the area of iron complexes/bioinorganic chemistry and related interface of chemistry.

3.5 References

(1)   Nam, W. *Acc. Chem. Res.* **2015**, *8*, 2415-2423.

(2)   Barman, P.; Upadhyay, P.; Faponle, A. S.; Kumar, J.; Nag, S. S.; Kumar, D.; Sastri, C. V.; de Visser, S. P. *Angew. Chem., Int. Ed.* **2016**, *55*, 11091-11095.

(3)   Jackson, T. A.; Rohde, J.-U.; Seo, M. S.; Sastri, C. V.; DeHont, R.; Stubna, A.; Ohta, T.; Kitagawa, T.; Munck, E.; Nam, W.; Que, L., Jr. *J. Am. Chem. Soc.* **2008**, *130*, 12394-12407.

(4)   Dhuri, S. N.; Cho, K.-B.; Lee, Y. M.; Shin, S. Y.; Kim, J. H.; Mandal, D.; Shaik, S.; Nam, W. *J. Am. Chem. Soc.* **2015**, *137*, 8623-8632

(5)   Lee, Y.-M.; Dhuri, S. N.; Sawant, S. C.; Cho, J.; Kubo, M.; Ogura, T.; Fukuzumi, S.; Nam, W. *Angew. Chem., Int. Ed.* **2009**, *48,* 1803-1806.

(6)   Dhuri, S. N.; Seo, M. S.; Lee, Y.-M.; Hirao, H.; Wang, Y.; Nam, W. Shaik, S. *Angew. Chem., Int. Ed.* **2008**, *47*, 3356-3359.

(7)   Dhuri, S. N.; Lee, Y.-M.; Seo, M. S.; Cho, J.; Narulkar, D. D.; Fukuzumi, S.; Nam, W. *Dalton Trans.* **2015**, *44*, 7634-7642.

(8)   Punniyamurthy, T.; Velusamy, S.; Iqbal, J. *J. Chem. Rev.* **2005**, *105*, 2329-2364.

(9)   Nam, W. *Acc. Chem. Res.* **2007**, *40*, 522-531.

(10) Shaik, S.; Lai, W.; Chen, H.; Wang, Y. *Acc. Chem. Res.* **2010**, *43*, 1154-1165.

(11) de Montellano, P. R. O. *Chem. Rev.* **2010**, *110*, 932-948.

(12) Wackett, L. P. *Enzyme Microb. Technol.* **2002**, *31*, 577-587.

(13) Horn, E. J.; Rosen, B. R.; Chen, Y.; Tang, J.; Chen, K.; Eastgate, M. D.; Baran, P. S. *Nature* **2016**, *533*, 77-81.

(14) Nakamura, A.; Nakada, M. *Synthesis* **2013**, *45*, 1421-1451.

(15) Garcia-Cabeza, A. L.; Moreno-Dorado, F. J.; Ortega, M. J.; Guerra, F. M. *Synthesis* **2016**, *48*, 2323-2342.

(16)   White, M. C. *Synlett* **2012**, *23*, 2746-2748.

(17)   Jazzar, R.; Hitce, J.; Renaudat, A.; Sofack-reutzer, J.; Baudoin, O. *Chem. -Eur. J.* **2010**, *16*, 2654-2672.

(18)   Groves, J. T. *J. Inorg. Biochem.* **2006**, *100*, 434-447.

(19)   Groves, J. T.; Haushalter, R. C.; Nakamura, M.; Nemo, T. E.; Evans, B. J. *J. Am. Chem. Soc.* **1981**, *103*, 2884-2886.

(20)   Groves, J. T.; Nemo, T. E. *J. Am. Chem. Soc.* **1983**, *105*, 6243-6248.

(21)   Meunier, B. *Chem. Rev.* **1992**, *92*, 1411-1456.

(22)   Costas, M.; Mehn, M. P.; Jensen, M. P.; Que, L., Jr. *Chem. Rev.* **2004**, *104*, 939-986.

(23)   Que, L., Jr. *Acc. Chem. Res.* **2007**, *40*, 493-500

(24)   Hitomi, Y.; Arakawa, K.; Funabiki, T.; Kodera, M. *Angew. Chem., Int. Ed.* **2012**, *124*, 3504-3508.

(25)   Talsi, E. P.; Bryliakov, K. P. Coord. *Chem. Rev.* **2012**, *256*, 1418-1434.

(26)   Zhang, Q.; Gorden, J. D.; Goldsmith, C. R. *Inorg. Chem.* **2013**, *52*, 13546-13556.

(27)   Lindhorst, A. C.; Haslinger, S.; Kuhn, F. E. *Chem. Commun.* **2015**, *51*, 17193-17212.

(28)   Oloo, W. N.; Que, L., Jr. *Acc. Chem. Res.* **2015**, *48*, 2612-2621.

(29)   Sankaralingam, M.; Lee, Y.-M.; Nam, W.; Fukuzumi, S. *Inorg. Chem.* **2017**, *56*, 5096-5104.

(30)   Cavani, F.; Teles, J. H. *Chem. Sus. Chem.* **2009**, *2*, 508-534.

(31)   Osterberg, P. M.; Niemeier, J. K.; Welch, C. J.; Hawkins, J. M.; Martinelli, J. R.; Johnson, T. E.; Root, T. W.; Stahl, S. S. *Org. Process. Res. Dev.* **2015**, *19*, 1537-1543.

(32)   Backvall, J.-E.; Modern Oxidation Methods, Wiley-VCH Verlag GmbH, Weinheim, **2004**.

(33)   Solomon, E. I.; Wong, S. D.; Liu, L. V.; Decker, A.; Chow, M. S. *Curr. Opin. Chem. Biol.* **2009**, *13*, 99-113.

(34) Abu-Omar, M. M.; Loaiza, A.; Hontzeas, N. *Chem. Rev.* **2005**, *105*, 2227-2252.

(35) Solomon, E. I.; Neidig, M. L. *Chem. Commun.* **2005**, *105*, 2227-2252.

(36) Chen, M. S.; White, M. C. *Science* **2007**, *318*, 783-787.

(37) Chen, M. S.; White, M. C. *Science* **2010**, *327*, 566-571.

(38) Gormisky, P. E.; White, M. C. *J. Am. Chem. Soc.* **2013**, *135*, 14052-14055.

(39) Chanda, A.; Popescu, D.-L.; de Oliveira, F. T.; Bominaar, E. L.; Ryabov, A. D.; Munck, E.; Collins, T. J. *J. Inorg. Biochem.* **2006**, *100*, 606-619.

(40) Sahu, S.; Goldberg, D. P. *J. Am. Chem. Soc.* **2016**, *138*, 11410-11428.

(41) Kovaleva, E. G.; Lipscomb, J. D. *Nat. Chem.* **2008**, *4*, 186-193.

(42) Pau, M. Y. M.; Lipscomb, J. D.; Solomon, E. I. *Proc. Natl. Acad. Sci. USA* **2007**, *104*, 18355-18362.

(43) Jasniewski, A. J.; Que, L., Jr. *Chem. Rev.* **2018**, *118*, 2554-2592.

(44) Huang, X.; Groves, J. T. *Chem. Rev.* **2018**, *118*, 2491-2553.

(45) Solomon, E. I.; Goudarzi, S.; Sutherlin, K. D. *Biochemistry* **2016**, *55*, 6363-6374.

(46) Wang, J.; Sun, H.; Zhao, X. S. *Catal. Today* **2010**, *158*, 263-268.

(47) Institute for Green Oxidation Chemistry, unpublished results.

(48) Collins, T. J. *Acc. Chem. Res.* **2002**, *35*, 782-790.

(49) Chanda, A.; de Oliveira, F. T.; Collins, T. J.; Munck, E.; Bominaar, E. L. *Inorg. Chem.* **2008**, *47*, 9373-9376.

(50) de Oliveira, F. T.; Chanda, A.; Banerjee, D.; Shan, X.; Mondal, S.; Que, L., Jr.; Bominaar, E. L.; Mu□nck, E.; Collins, T. J. *Science* **2007**, *315*, 835-838.

(51) Collins, T. J.; Walter, C. *Little green molecules Sci. Am.* **2006**, *294*, 82-90.

(52) Collins, T. J.; Gordon-Wylie, S. W.; Bartos, M. J.; Horwitz, C. P.; Woomer, C. G.; Williams, S. A.; Patterson, R. E.; Vuocolo, L. D.; Paterno, S. A.; Strazisar, S. A.; Peraino, D. K.; Dudash, C. A.; In Green chemistry: environmentally benign chemical

syntheses and processes, Anastas, P. T.; Williamson TC, Eds. Oxford University Press: Oxford, **1998** pp 46-71.

(53) Pattanayak, S.; Jasniewski, J. A.; Rana, A.; Draksharapu, A.; Singh, K. K.; Weitz, A.; Hendrich, M.; Que, L., Jr.; Dey, A.; Gupta, S. S. *Inorg. Chem.* **2017**, *56*, 6352-6361.

(54) Nam, W. *Acc. Chem. Res.* **2015**, *48*, 2415-2423.

(55) Ghosh, A.; de Oliveira, F. T.; Yano, T.; Nishioka, T.; Beach, E. S.; Kinoshita, I.; Munck, E.; Ryabov, A. D.; Horwitz, C. P.; Collins, T. J. *J. Am. Chem. Soc.* **2005**, *127*, 2505-2513.

(56) Hong, S.; Sutherlin, K. D.; Park, J.; Kwon, E.; Siegler, M. A.; Solomon, E. I.; Nam, W. *Nat. Commun.* **2014**, *5*, 5440-5447.

(57) Fan, R.; Serrano-Plana, J.; Oloo, W. N.; Draksharapu, A.; Delgado-Pinar, E.; Company, A.; MartinDiaconescu, V.; Borrell, M.; Lloret-Fillol, J.; Garcia-Espana, E.; Guo, Y.; Bominaar, E.; Que L.; Jr.; Costas, M.; Munck, E. *J. Am. Chem. Soc.* **2018**, *140*, 3916-3928.

(58) Ghosh, M.; Pattanayak, S.; Dhar, B. B.; Singh, K. K.; Panda, C.; Gupta, S. S. *Inorg. Chem.* **2017**, *52*, 10852-10856.

(59) Zou, G.; Jing, D.; Zhong, W.; Zhao, F.; Mao, L.; Xu, Q.; Xiao J.; Yin, D. *RSC. Adv*. **2016**, *6*, 3729-3734.

(60) Boudjema, S.; Vispe, E.; Choukchou-Braham, A.; Mayoral, J. A.; Bachir, R.; Fraile, J. M. *RSC. Adv.* **2015**, *5*, 6853-6863.

(61) Ray, K.; Pfaff, F.; Wang, B.; Nam, W. *J. Am. Chem. Soc.* **2014**, *136*, 13942-13958.

(62) Cho, J.; Sarangi, R.; Nam, W. *Acc. Chem. Res.* **2012**, *45*, 1321-1330.

(63) Kang, H.; Cho, J.; Cho, K.-B.; Nomura, T.; Ogura, T.; Nam, W. *Chem. -Eur. J.* **2013**, *19*, 14119-14125.

(64) Cho, J.; Kang, H. Y.; Liu, L. V.; Sarangi, R.; Solomon, E. I.; Nam, W. *Chem. Sci.* **2013**, *4*, 1502-1508.

(65) Rohde, J.-U.; In, J.-H.; Lim, M. H.; Brennessel, W. W.; Bukowski, M. R.; Stubna, A.; Munck, E.; Nam, W.; Que, L., Jr. *Science* **2003**, *299*, 1037-1039.

(66) Seo, M. S.; Kim, N. H.; Cho, K.-B.; So, J. E.; Park, S. K.; Clemancey, M.; Garcia-Serres, R.; Latour, J.-M.; Shaik, S.; Nam, W. *Chem. Sci.* **2011**, *2*, 1039-1045.

(67) Rohde, J.-U.; Stubna, A.; Bominaar, E. L.; Münck, E.; Nam, W.; Que, L., Jr. *Inorg. Chem.* **2006**, *45*, 6435-6445.

(68) Pandey, B.; Jaccob, M.; Rajaraman, G. *Chem. Commun.* **2017**, *53*, 3193-3196.

(69) Bell, S. R.; Groves, J. T. *J. Am. Chem. Soc.* **2009**, *131*, 9640-9641.

(70) Fukuzumi, S.; Morimoto, Y.; Kotani, H.; Naumov, P.; Lee, Y.-M.; Nam, W. *Nat. Chem.* **2010**, *2*, 756-759.

(71) Ansari, A.; Kaushik, A.; Rajaraman, G. *J. Am. Chem. Soc.* **2013**, *135*, 4235-4249.

(72) Ansari, M.; Vyas, N.; Ansari, A.; Rajaraman, G. *Dalton Trans.* **2015**, *44*, 15232-15243.

(73) Ansari, A.; Ansari, M.; Singha, A.; Rajaraman, G. *Chem. -Eur. J.* **2017**, *23*, 10110-10125.

(74) Kumar, R.; Ansari, A.; Rajaraman, G. *Chem. -Eur. J.* **2018**, *24*, 6660-6860.

(75) Horn, E.; Rosen, B.; Chen, Y.; Tang, J.; Chen, K.; Eastgate, M.; Baran, P. *Nature* **2016**, *533*, 77-81.

(76) Yachandra, V.; Sauer, K.; Klein, M. *Chem. Rev.* **1996**, *96*, 2927-2950.

(77) Karlsson, A.; Parales, J.; Parales, R.; Gibson, D.; Eklund, H.; Ramaswamy, S. *Science* **2003**, *299*, 1039-1042.

(78) Frisch, M. J.; Trucks, G. W.; Schlegel, H. B.; Scuseria, G. E.; Robb, M. A.; Cheeseman, J. R.; Scalmani, G.; Barone, V.; ennucci, B.; Petersson, G. A.; Nakatsuji,

H.; Caricato, M.; Li, X.; Hratchian, H. P.; Izmaylov, A. F.; Bloino, J.; Zheng, G.; Sonnenberg, J. L.; Hada, M.; Ehara, M.; Toyota, K.; Fukuda, R.; Hasegawa, J.; Ishida, M.; Nakajima, T.; Honda, Y.; Kitao, O.; Nakai, H.; Vreven, T.; Montgomery, J. A. Jr.; Peralta, J. E.; Ogliaro, F.; Bearpark, M.; Heyd, J. J.; Brothers, E.; Kudin, K. N.; Staroverov, V. N.; Keith, T.; Kobayashi, R.; Normand, J.; Raghavachari, K.; Rendell, A.; Burant, J. C.; Iyengar, S. S.; Tomasi, J.; Cossi, M.; Rega, N.; Millam, J. M.; Klene, M.; Knox, J. E.; Cross, J. B.; Bakken, V.; Adamo, C.; Jaramillo, J.; Gomperts, R.; Startmann, R. E.; Yazyev, O.; Austin, A. J.; Cammi, R.; Pomelli, C.; Ochterski J. W., Martin, R. L.; Morokuma, K.; Zakrzewski, V. G.; Voth, G. A.; Salvador, P.; Dannenbergy, J. J.; Dapprich, S.; Daniels, A. D.; Farkas, O.; Foresman, J. B.; Ortiz, J. V.; Cioslowski, J.; Fox, D. J.; GAUSSIAN 09 Revision(A.01), Gaussian, Inc, Wallingford, CT (2009)

(79) Grimme, S. J. *Comput. Chem.* **2006**, *27*, 1787-1799.

(80) Dunning, T. H. Jr.; Hay, P. J.; In Modern Theoretical Chemistry (Ed: Schaefer, H), Plenum, New York, **1976** Vol. 3.

(81) Hay, P. J.; Wadt, W. R. *J. Chem. Phys.* **1985**, *82*, 270-283.

(82) Hay, P. J.; Wadt, W. R. *J. Chem. Phys.* **1985**, *82*, 299-310.

(83) Wadt, W. R.; Hay, P. J. *J. Chem. Phys.* **1985**, *82*, 284-298.

(84) Schaefer, A.; Horn, H.; Ahlrichs, R. *J. Chem. Phys.* **1992**, *97*, 2571-2577.

(85) Schaefer, C.; Huber, C.; Ahlrichs, R. *Chem. Phys.* **1994**, *100*, 5829-5835.

(86) Jomroz, M. H.; Vibrational Energy Distribution Analysis, VEDA4, Warsaw, **2004**.

(87) James, C.; Raj, A. A.; Reghunathan, R.; Jayakumar, V. S.; Joe, I. H.; *J. Raman Spectrosc.* **2006**, *37*, 1381-1392.

(88) Liu, J.; Chen, Z.; Yuan, S. J *Zhejiang Univ. Sci. B.* **2005**, *6*, 584-589.

(89) Noodleman, L. *J. Chem. Phys.* **1981**, *74*, 5737-5743.

(90) Noodleman, L.; Davidson, E. R. *Chem. Phys.* **1986**, *109*, 131-143.

(91) Vaska, L. *Acc. Chem. Res.* **1976**, *9*, 175-183.

(92) Dickman, M. H.; Pope, M. T. *Chem. Rev.* **1994**, *94*, 569-584.

(93) Shan, X.; Que, L., Jr. *Proc. Natl. Acad. Sci. USA* **2005**, *102*, 5340-5345.

(94) Momenteau, M.; Reed, C. A. *Chem. Rev.* **1994**, *94*, 659-698.

(95) Kundu, S.; Matito, E.; Walleck, S.; Pfaff, F. F.; Heims, F.; Babay, R.; Luis, J. M.; Company, A.; Braun, B.; Glaser, T.; Ray, K. *Chem. -Eur. J.* **2012**, *18*, 2787-2791.

(96) Cramer, C. J.; Tolman, W. B.; Theopold, K. H.; Rheingold, A. L. *Proc. Natl. Acad. Sci. USA*, **2003**, *100*, 3635-3640.

(97) Ansari, A.; Jayapal, P.; Rajaraman, G. *Angew. Chem., Int. Ed.* **2015**, *127*, 564-568.

(98) Seo, M. S.; Kim, J. Y.; Annaraj, J.; Kim, Y.; Lee, Y.-M., Kim, S. J.; Kim, J. Nam, W. *Angew. Chem., Int. Ed.* **2007**, *46*, 377-380.

(99) Grapperhaus, C. A.; Mienert, B.; Bill, E.; Weyhermüller, T.; Wieghardt, K. *Inorg. Chem.* **2000**, *39*, 5306-5317.

(100) Monika, Ansari, A. *New J. Chem.* **2020**, *44*, 7998-8009.

(101) Ansari, A.; Rajaraman, G. *Phys. Chem. Chem. Phys.* **2014**, *16*, 14601-14613.

(102) Kundu, S.; Thompson, J. V. K.; Ryabov, A. D.; Collins, T. J. *J. Am. Chem. Soc.* **2011**, *133*, 18546-18549.

(103) Stoian, S.; Xue, G. Q.; Bominaar, E. L.; Que, L., Jr.; Munck, E. *J. Am. Chem. Soc.* **2014**, *136*, 1545-1558.

(104) Fukuzumi, S.; Mandal, S.; Mase, K.; Ohkubo, K.; Park, H.; Benet-Buchholz, J.; Nam, W.; Llobet, A. *J. Am. Chem. Soc.* **2012**, *134*, 9906-9909

(105) Makhlynets, O. V.; Das, P.; Taktak, P.; Flook, M.; Mas-Ballesté, R.; Rybak-Akimova, E. V.; Que, L., Jr. *Chem. -Eur J.* **2009**, *15*, 13171-13180.

(106) Makhlynets, O. V.; Rybak-Akimova, E. V. *Chem. -Eur J.* **2010**, *16*, 13995-14006.